Barium isotopes in mid-ocean ridge hydrothermal vent fluids: a source of isotopically heavy Ba to the ocean

Yu-Te Hsieh[a,*] , Luke Bridgestock[a], Peter P. Scheuermann[b], William E. Seyfried Jr[b]., and Gideon M. Henderson[a]

[a]Department of Earth Sciences, University of Oxford, UK

[b]Department of Earth and Environmental Sciences, University of Minnesota, USA

Highlights:

1. MOR vent fluids show the largest range of $\delta^{138/134}$Ba seen so far in marine systems.
2. Endmember vent fluid $\delta^{138/134}$Ba values are the same as those of the source rocks.
3. Barite precipitation leads to high $\delta^{138/134}$Ba values in vent fluids.
4. Hydrothermal Ba input explains the non-conservative $\delta^{138/134}$Ba seen in deep waters.
5. Hydrothermal input contributes 3-9% of the Ba in some Atlantic deep waters.

Manuscript for submission to Geochemica et Cosmochimica Acta

***Corresponding author: yu-te.hsieh@earth.ox.ac.uk**

Abstract

Mid-ocean ridge (MOR) hydrothermal vent fluids are enriched with dissolved barium, but due to barite ($BaSO_4$) precipitation during mixing between Ba-bearing vent fluids and SO_4-bearing seawater, the magnitude of hydrothermal Ba input to the ocean remains uncertain. Deep-ocean Ba isotopes show evidence for non-conservative behavior, which might be explained by input of isotopically heavy hydrothermal Ba. In this study we present the first Ba isotope data in mid-ocean ridge hydrothermal vent fluids and particles from systems on the Mid-Atlantic Ridge (Rainbow 36°N and TAG 26°N), the East Pacific Rise (EPR9-10°N and 13°N) and the Juan de Fuca Ridge (MEF and ASHES). The vent fluids display a wide range of dissolved Ba concentrations from 0.43 to 97.9 μmol/kg and $\delta^{138/134}$Ba values from -0.26 to +0.91 ‰, but are modified relative to initial composition due to precipitation of barite. Calculated endmember vent fluid $\delta^{138/134}$Ba values, prior to barite precipitation, are between -0.17 and +0.09 ‰, consistent with the values observed in oceanic basalts and pelagic sediments. Water-rock interaction inside the hydrothermal system appears to occur without isotope fractionation. During subsequent venting and mixing with seawater, barite precipitation preferentially removes isotopically light Ba from vent fluids with a fractionation factor of $\Delta^{138/134}Ba_{hyd\text{-}barite\text{-}fluid} = -0.35 \pm 0.10$ ‰ (2SE, n=2). Based on knowledge of barite saturation and isotope fractionation during precipitation, the effective hydrothermal Ba component that mixes with seawater after all barite precipitation has taken place can be calculated: $\delta^{138/134}Ba_{hyd} = +1.7 \pm 0.7$ ‰ (2SD). This value is isotopically heavier than deep ocean waters and may explain the observed non-conservative of Ba isotopes. These new constraints on hydrothermal Ba compositions enable the hydrothermal input of Ba to Atlantic deep waters to be assessed at ≈ 3 – 9 % of the observed Ba. Barium isotopes might be used as a tracer to

reconstruct the history of hydrothermal Ba inputs and seawater SO_4 concentrations in the past.

1. Introduction

Mid-ocean ridge (MOR) hydrothermal systems play an important role in determining seawater chemistry (Von Damm, 1990; Elderfield and Schultz, 1996; German and Von Damm, 2003; Tivey, 2007; German and Seyfried et al. 2014; Humphirs and Klein, 2018; Coogan et al., 2019). Hydrothermal systems are a source of some elements to seawater (e.g. Fe, Mn and Li) and a sink for others (e.g. Mg and SO_4). Hydrothermal vent fluids are enriched in Ba (1 ~ 119 μmol/kg) by up to 1000 times relative to seawater (0.03 ~ 0.2 μmol/kg) (e.g. Butterfield et al., 1994; Charlou et al., 1996; Von Damm, 1995; Kumagai et al., 2008; Seyfried et al. 2011).

Many processes control the hydrothermal flux of Ba into the ocean. Water-rock interaction releases Ba from source rocks to vent fluids at elevated pressures and temperatures (Von Damm et al., 1985). These source rocks contain Ba at the level of [Ba] = 3.9 – 160.3 ppm in oceanic basalts (Gale et al., 2013) and [Ba] = 350 – 6230 ppm in marine sediments (Li and Schoonmaker, 2003), explaining the high Ba concentration values in initial vent fluids. Mixing between these vent fluids and SO_4-bearing seawater, however, leads to barite ($BaSO_4$) precipitation (e.g. Shikazono, 1994; Hanor, 2000; Seyfried et al. 2003; Jamieson et al., 2016; Gartman et al., 2019), which removes Ba from vent fluids and reduces hydrothermal Ba input to seawater. Therefore, despite the fact that Ba concentrations in vent fluids are several orders of magnitude higher than in seawater, the ‘effective’ hydrothermal Ba input to the ocean is smaller and remains uncertain.

Barium isotopes have recently been studied as a new tracer to understand the oceanic Ba cycle (Horner et al., 2015; Hsieh and Henderson, 2017; Bates et al., 2017; Bridgestock et al., 2018; Crockford et al., 2019; Cao et al., 2020). In general, seawater $\delta^{138/134}$Ba values range from +0.22 to +0.65 ‰ in the global oceans. The deep Pacific Ocean has higher Ba concentrations (> 0.1 μmol/kg) and lighter $\delta^{138/134}$Ba values (< +0.3‰) than the Atlantic Ocean. The main process controlling observed variations in seawater $\delta^{138/134}$Ba is barite formation and dissolution. This barite precipitation preferentially removes light Ba isotopes from solutions into solid phases (e.g. von Allmen et al., 2010; Böttcher et al., 2018).

The Ba isotope composition $\delta^{138/134}$Ba of major inputs and outputs of Ba to the ocean has been assessed. The main input to the ocean is from rivers and is isotopically light, ranging from -0.06 to +0.46 ‰ (Cao et al., 2020; Hsieh and Henderson, 2017; Gou et al., 2020). Estuaries also play an important role in the riverine Ba isotope compositions through adsorption and desorption of Ba between suspended particles and the dissolved phase (Gou et al., 2020). The main output is into marine sediments, particularly as precipitated barite, and is also isotopically lighter than seawater, ranging from -0.21 to +0.11 ‰ in suspended particles and pelagic sediments (Horner et al., 2017; Bridgestock et al., 2018; Crockford et al., 2019). As yet, there are no available data to constrain Ba isotope compositions in vent fluids.

The degree to which Ba isotopes behave conservatively in the deep ocean is uncertain. Bates et al. (2017) suggested that Ba isotopes in deep waters are mostly conservative during the mixing between North Atlantic Deep Water (NADW, $\delta^{138/134}$Ba ≈ +0.45‰) and Antarctic Bottom Water (AABW, $\delta^{138/134}$Ba ≈ +0.25‰), but Hsieh and Henderson (2017) identified evidence for non-conservative mixing in deep waters, with deviations towards higher $\delta^{138/134}$Ba values than the conservative mixing

100 trend, particularly at depths of 2000 – 3000m (Fig. 1). Hydrothermal Ba inputs may
101 be an explanation for such non-conservative behavior.

102 In this study, we present the first Ba isotope data in hydrothermal vent fluids
103 from 6 hydrothermal systems in both the Atlantic and Pacific Oceans to establish the
104 relationship between vent fluid Ba isotope compositions and hydrothermal processes
105 (e.g. water-rock interaction and barite precipitation). We pair the dissolved and
106 particulate Ba data from the same hydrothermal vent fluids to understand the
107 correlation between barite precipitation and Ba isotope fractionation in hydrothermal
108 systems.

109

110 **2. Materials and methods**

111 **2.1. Hydrothermal vent fluids and particles**

112 All the vent fluid and particle samples analyzed in this study were obtained by
113 the University of Minnesota co-authors over the past 15 years. The fluid samples (21
114 focused-flow and 10 diffuse-flow) were selected from 6 different hydrothermal
115 systems with distinct geologic settings along the mid-ocean ridges in both the Atlantic
116 and Pacific Oceans. Sites included are from the slow-spreading Mid-Atlantic Ridge
117 (MAR): Rainbow (36^{o}N, ultramafic-hosted) and Trans Atlantic Geotraverse (TAG,
118 26^{o}N, active mound); the fast-spreading East Pacific Rise (EPR): 9-10^{o}N and 13^{o}N
119 (basalt-hosted); the intermediate-spreading Juan de Fuca Ridge (JdFR) in the
120 Northeast Pacific: Main Endeavor Field (MEF) (sediment-influenced) and ASHES
121 vent field, Axial Caldera (ASHES) (Fig. 2). Diffuse-flow samples generally refer to
122 the MOR discharged vent fluids at low temperature (relative to the high temperature
123 focused-flow, > 250^{o}C), low flow rates and broad spatial distributions (Bemis et al.,
124 2012). In this study, only 3 of the 10 diffuse-flow samples have sufficient Ba for

125 isotope analysis. To assess the controls of Ba isotopes in diffuse-flow vent fluids,
126 more data will be required.

127 Vent fluid samples were collected in a titanium syringe-type gas-tight
128 sampling device (Seewald et al., 2002; Wu et al., 2015). Initial ship-board processing
129 of fluids occurred within hours of sample recovery from the seafloor. In general,
130 subsamples were taken under pressure from each bottle for determination of pH (at
131 25□C), H_2S, major dissolved anions and cations, and trace metals. The trace metal
132 aliquot was immediately acidified with high-purity HCl (Optima, Fisher Chemical) to
133 pH ~1. A fraction of this subsample (200 μL) was preserved in pre-weighed and acid-
134 cleaned polyethylene vials before sending to Oxford for analysis of Ba isotopes.

135 Precipitates that formed in the samplers upon cooling and mixing with
136 entrained seawater were rinsed with Milli-Q water, collected on a 0.2 μm nylon filter
137 and subsequently re-dissolved in HCl/HNO_3 (ULTREX, J.T. Baker). These
138 precipitates are commonly called "dregs", and usually contain high levels of transition
139 metals (e.g. Cu, Fe, and Zn). Based on the metal contents, the mineralogy of dregs is
140 mainly sulfides (e.g. chalcopyrite and sphalerite) with other trace metals, such as As,
141 Mo and Ba (Metz and Trefry, 2000; Rouxel et al., 2008; Yucel et al., 2011; Gartman
142 et al., 2014; Gartman et al., 2018). Scanning electron microscopy (SEM) images show
143 that Ba exists as barite, surrounded by sulfides, in the particles precipitated in vent
144 fluids (Gartman et al., 2018). Precipitation of dregs reduces the concentrations or
145 causes isotope fractionation in these elements from the original fluids (Seyfried et al.,
146 2003; Rouxel et al., 2008; James et al., 2014). The amount of metals measured in the
147 dregs was therefore recombined with metals that remained in solution to obtain a
148 complete metal inventory of the vent fluids prior to collection. Dregs are not available
149 for 10 vent fluid samples (out of 31) reported here. These samples are mostly diffuse-

150 flow type with no precipitation of dregs, except for two focused-flow samples (4744-1
151 and 4744-2) where their dregs were not kept and had no recorded Ba data. All fluid
152 samples without dregs are reported as uncorrected data only.

153 Sample ID (including sample years and submersible dive numbers), vent type,
154 location, and names are provided in Table 1, as are references to published data and
155 procedures that provide information critical to the broader interpretation of the Ba
156 data reported here. Vent fluid chemistries in these and other marine hydrothermal
157 systems have been well documented (e.g. Campbell et al., 1988; Butterfield et al.,
158 1990; Von Damm, 1990; Von Damm, 2000; Charlou et al., 2002; Douville et al.,
159 2002; Seyfried et al. 2003; Seyfried et al., 2011; Fornari et al., 2012). Most of the
160 fluid samples provided for this study have been analyzed and discussed for other trace
161 elements and isotopes in previous studies (Foustoukos and Seyfried, 2007;
162 Foustoukos et al., 2009; Pester et al., 2011; Seyfried et al., 2011; Pester et al., 2014;
163 Syverson et al., 2017; Scheuermann et al., 2018).

164

165 **2.2. Elemental concentrations analysis**

166 Most of the vent fluids and dregs samples have been previously analyzed for
167 major and trace elements/species (Mg, Ca, Ba, Cl and SO_4) by ion chromatography
168 (IC) and inductively coupled plasma optical emission spectrometry (ICP-OES) at the
169 University of Minnesota. All the vent fluid Ba concentrations were measured by
170 isotope dilution (ID) thermal ionization mass spectrometer (TIMS) and quadrupole
171 (Quad) ICP-MS at the University of Oxford. The concentration unit of fluid and dregs
172 [Ba] was normalized to the weight of fluid ($[Ba]_{fluid}$ = fluid Ba μmol/fluid kg; $[Ba]_{dregs}$
173 = dregs Ba μmol/fluid kg). For comparison, the data of [Ba] between ID-TIMS and
174 Quad-ICP-MS show agreement within 1-11% (Fig. S1). Therefore, we mainly use the

ID-TIMS [Ba] data in the discussion unless otherwise specified. Overall, the precision of the elemental concentrations is around 1-3 % RSD. The total Ba concentration was corrected ($[Ba]_{corr}$) by the sum of Ba concentrations in dissolved fluids and dregs:

$$[Ba]_{corr} = [Ba]_{fluid} + [Ba]_{dregs} \quad (1)$$

2.3. Barium isotope analyses

All the fluid solution samples were prepared and analyzed for Ba isotopes and Ba concentrations using ID-TIMS at the University of Oxford. In addition to the fluid samples, two of the dregs samples from MEF and ASHES were also analyzed for Ba isotopes (Table 2). The Ba isotope methods were adapted from previous studies (Hsieh and Henderson, 2017; Bridgestock et al., 2018). In brief, sample solutions, containing ~200 ng of Ba or maximum 200 μL fluid, were weighed, acidified and spiked with ^{137}Ba-^{135}Ba double spike. The samples were dried and re-dissolved in 1mL 3M HCl before purification by cation exchange chromatography (AG50-X8, 200-400 mesh). The overall procedure blank is < 0.1 ng of Ba (n = 3). Barium isotope analyses were performed on a Thermo Finnigan Triton TIMS at the University of Oxford. In this study, Ba isotopic compositions are reported as the δ-notation $\delta^{138/134}$Ba (‰) relative to the National Institute of Standards and Technology (NIST) 3104a standard:

$$\delta^{138/134}\text{Ba (‰)} = \left(\frac{^{138}\text{Ba}/^{134}\text{Ba}_{sample}}{^{138}\text{Ba}/^{134}\text{Ba}_{NIST3104a}} - 1\right) \times 1000 \quad (2)$$

For comparison, data reported in $\delta^{137/134}$Ba in some previous studies have been converted to $\delta^{138/134}$Ba by multiplying by 1.33.

Standards and samples generally show an internal precision between 0.01 and 0.02 ‰ (± 2SE, n = 540) during each isotope analysis. The long-term (external) precision and accuracy are monitored with a secondary Ba standard NBS-127 over

two years, $\delta^{138/134}$Ba = -0.29 ± 0.02 ‰ (± 2SD, n = 14), which is in agreement with published values in previous studies (Horner et al., 2017; Crockford et al., 2019). We use the repeatability of these standard measurements to assess uncertainty of single measurement, which is generally quoted in this paper as ±0.02‰. Most measurements had similar or better internal uncertainty (0.01-0.02 ‰, ± 2SE) but a small number, with low Ba contents, show larger internal uncertainty, up to 0.08 ‰ (±2 SE). For these samples, we use the internal uncertainty from their measurement.

3. Results

The hydrothermal vent fluids display a wide range of Ba concentrations from 0.43 to 97.9 μmol/kg and $\delta^{138/134}$Ba values from -0.26 to +0.91 ‰, including both dregs corrected and uncorrected data, in selected hydrothermal fluids from six different vent fields (Table 1; Fig. 3). For comparison, temperature, pH, Mg, Cl, Ca and SO_4 data are provided in Table 1 and Table S1, and seawater data from the North Atlantic (Bates et al., 2017; Hsieh and Henderson, 2017) and North Pacific (Geyman et al. 2019) are also provided. No significant relationship was found between the $\delta^{138/134}$Ba values and temperature, pH, [Mg], [SO_4], [Ca] or [Cl] (all $r^2 < 0.1$). The fluid data show a predictable linear relationship between SO_4 and Mg concentrations, which suggests a conservative mixing between seawater and endmembers components of the vent fluids (Fig. 3a). In contrast, Ba concentrations broadly decrease with increasing SO_4 concentrations due to seawater mixing (Fig. 3b). However, the relationship between Ba and SO_4 concentrations is not linear, which indicates that Ba is removed from solution during the mixing. The fluid $\delta^{138/134}$Ba compositions broadly increase with decreasing Ba concentrations, but this

224 relationship cannot be explained by conservative mixing between seawater and the
225 endmember fluids either (Fig. 3c).

226 Different hydrothermal systems show a wide range of dissolved Ba isotope
227 compositions $\delta^{138/134}$Ba and [Ba] (Table 1; Fig. 3c). Vent fluids from the ultramafic-
228 hosted Rainbow hydrothermal field (36^{o}N, MAR) show $\delta^{138/134}$Ba values from -0.26
229 to +0.36 ‰, associated with a large gradient of [Ba] changing from 4.54 to 97.9
230 μmol/kg. In the basalt-hosted EPR, the vent fluids from EPR 9-10^{o}N and EPR 13^{o}N
231 show diverse $\delta^{138/134}$Ba values from +0.02 to +0.40 ‰ with a range of [Ba] from 0.43
232 to 14.1 μmol/kg. In the JdFR, the $\delta^{138/134}$Ba value is generally much heavier in the
233 MEF and ASHES vent fluids (+0.40 to +0.91 ‰) than is the case for the other vent
234 fluids discussed, while the Ba concentrations (1.65 to 46.1 μmol/kg) are not hugely
235 different from the others.

236 Particulate (dregs) Ba concentrations show a wide range from below < 0.01
237 (below detection limit) to 41.2 μmol/kg. The sum of dregs Ba and dissolved fluid Ba
238 indicates the total content of Ba in the fluids, as calculated by equation 1 (Table 1).
239 The fraction of dregs Ba ranges from 2 to 83% of the total Ba. The dregs Ba isotopic
240 compositions $\delta^{138/134}$Ba in two available samples are -0.11 ± 0.02 ‰ and +0.08 ± 0.08
241 ‰, and both values are significantly lighter than their fluid $\delta^{138/134}$Ba values (Table 2).
242 For comparison, the observed $\delta^{138/134}$Ba compositions in hydrothermal barites also
243 show light values (-0.04 and -0.08 ‰, Crockford et al., 2019). The dregs isotope data
244 suggest that precipitation in the samplers has preferentially removed isotopically light
245 Ba from vent fluids, and that needs to be considered for the correction of $\delta^{138/134}$Ba
246 values in the vent fluids (see Discussion 4.2). The dregs corrected and uncorrected
247 [Ba] and $\delta^{138/134}$Ba data are both reported in Table 1 for comparison, but the following
248 discussion is mainly based on the corrected data unless otherwise specified.

4. Discussion

4.1. Barite saturation and precipitation during fluid-seawater mixing

Vent fluid Ba and SO_4 concentrations show that Ba is removed during mixing with seawater (Fig. 3b). Such a correspondence has been observed in previous studies and has been explained by barite ($BaSO_4$) precipitation (Von Damm, 1995; Seyfried et al. 2003). Barite is one of the most common minerals formed during the mixing of Ba-bearing hydrothermal vent fluids and SO_4-bearing seawater (Shikazono, 1994; Hanor, 2000; Jamieson et al., 2016; Gartman et al., 2019). Barite precipitation also often occurs during the sampling of high-temperature vent fluids as a result of seawater entrainment in the samplers, which has caused difficulty in determining the fluid endmember Ba concentrations (Butterfield and Massoth, 1994; Von Damm, 1995; Seyfried et al. 2003; Seyfried et al. 2011). Barite precipitation can also be induced by conductive cooling; reducing temperature decreases barite solubility and hence increases barite precipitation (Blount, 1977; Jamieson et al., 2016; Gartman et al., 2019).

Barite solubility experiments and thermodynamic models have been used to study Ba and SO_4 chemistry and assess barite saturation in different marine environments (Church and Wolgemuth, 1972; Blount, 1977; Monnin and Galinier, 1988; Monnin, 1999; Monnin et al. 1999; Monnin et al. 2001). In this study, we apply the model of Monnin (1999) to calculate the barite solubility product (K_{sp}), activity coefficient (γ_{BaSO4}) and barite saturation index (Ω_{barite}) in the fluid samples under the condition of mixing with deep seawater (1^{o}C and 500 bar):

$$\Omega_{barite} = IAP/K_{sp} \quad (3)$$

where IAP is the ionic activity product:

$$IAP = [Ba^{2+}]\cdot[SO_4^{2-}]\cdot \gamma^2_{BaSO4} \quad (4)$$

where $[Ba^{2+}]$ and $[SO_4^{2-}]$ are the fluid Ba and SO_4 mole concentrations. The model parameters are $LogK_{sp} = -9.957$ and $\gamma_{BaSO4} = 0.1442$ (Monnin, 1999).

The modeled curves of Ba and SO_4 concentrations at the equilibrium condition $\Omega_{barite} = 1$ are plotted in Fig. 3b and the calculated Ω_{barite} values are reported in Table S1. Most of the samples after the dregs correction are above the curve and the Ω_{barite} values are greater than or close to 1, which implies that the fluid samples are mostly supersaturated with respect to barite, except for one sample in EPR 9-10^{o}N (Ω_{barite} = 0.9). Given that the Ba concentration of this sample is higher than in seawater, where the observed Ω_{barite} value is undersaturated, this suggests low degrees of seawater (and therefore sulfate) entrainment during the sampling. As the process of venting evolves, barite precipitation can still happen with increased seawater mixing. The calculated saturation index Ω_{barite} is likely to be overestimated in this study due to the underestimate of solubility, particularly for the high temperature vent fluids. Thermodynamic models show that barite K_{sp} decreases with increasing temperature, but due to ion interactions and speciation changes, the solubility increases with increasing temperature in NaCl bearing fluids (Blount, 1977; Monnin 1999). Nevertheless, the chosen condition (1^{o}C and 500 bar) is likely to represent the end point of barite precipitation in hydrothermal plumes mixing with seawater, which provides constraints on the barite precipitation during the entire process and hence the effective input of hydrothermal Ba to the ocean.

4.2. Precipitates in the fluids: correction and assessment of fractionation

Precipitation of "dregs" from hydrothermal vent fluid often occurs in the samplers during cooling and mixing with seawater. Although the mineralogy of dregs

299 is mainly metal sulfides (Metz and Trefry, 2000; Rouxel et al., 2008; Yucel et al.,
300 2011; Gartman et al., 2014; Gartman et al., 2018), Ba sulfide (BaS) is highly soluble
301 in water, which makes BaS unlikely to be the host for Ba in the dregs. One previous
302 study has shown that Ba exists as barite, surrounded by sulfides, in the particles
303 precipitated in vent fluids (Gartman et al., 2018). Ba is also commonly observed as
304 barite in sulfide-rich deposits and chimneys in hydrothermal systems (Koski et al.,
305 1994; Shikazono, 1994; Tivey, 2007; James et al., 2014; Jamieson et al., 2016).
306 Although these do not exclude the possibility of having some Ba scavenged onto
307 other mineral surfaces (e.g. MnS) when samples are undersaturated for barite, barite
308 seems to be the most likely mineral to host the majority of Ba in the dregs when
309 samples are supersaturated.

310 Correction for dregs is required to assess the original composition of the fluid
311 prior to precipitation. The calculation also enables an assessment of the isotope
312 fractionation occurring during precipitation. Initial fluid Ba isotope compositions
313 were corrected for precipitation of dregs using the analyses of the two dregs samples
314 (Table 2; calculation details in supplementary material S1).

315 The average value of calculated $\Delta^{138/134}Ba_{dregs\text{-}fluid}$ is -0.35 ± 0.10 ‰ (2SE,
316 n=2). This agrees with values from barite precipitation in previous experimental
317 studies ($\Delta^{138/134}Ba_{barite\text{-}fluid}$ = -0.34 ± 0.09 ‰, von Allmen et al., 2010), consistent with
318 barite being the major phase hosting Ba in the dregs. The results from previous
319 experiments, conducted between 4 and 80^{o}C, have shown that Ba isotope
320 fractionation has no temperature dependence in barite precipitation (Von Allmen et al,
321 2010; Böttcher et al., 2018). The similarity of observed fractionation at the higher
322 temperatures of dregs precipitation implies that this temperature independence may
323 hold to the in situ temperature of vent fluids (~350^{o}C). Considering the uncertainties,

the hydrothermal barite Ba isotope fractionation factor is quite similar to that in pelagic barite ($\Delta^{138/134}Ba_{pelagic\text{-}barite\text{-}seawater}$ ranging from -0.40 to -0.58 ‰, Hsieh and Henderson, 2017; Horner et al., 2017; Bridgestock et al., 2018). Although the fractionation factor in pelagic barite may be slightly larger, it possibly reflects the different precipitation conditions and environment (e.g. microenvironment and bacteria for pelagic barite, Bishop, 1998; Martinez-Ruiz et al., 2018).

The corrected $\delta^{138/134}Ba$ values in the fluids were made by using the measured $\delta^{138/134}Ba_{fluid}$, $[Ba]_{fluid}$ and $[Ba]_{dregs}$ from each sample (Table 1; equation S3), assuming that barite is the major phase hosting Ba in dregs and that it has a constant fractionation factor ($\Delta^{138/134}Ba_{hyd\text{-}barite\text{-}fluid}$ = -0.35 ± 0.10 ‰). Ba isotope compositions in four fluid samples are not corrected for dregs due to the lack of dregs [Ba] data. The fractionation factor can also be used in the Ba isotope fractionation model to explain the distribution of hydrothermal vent fluid $\delta^{138/134}Ba$ values controlled by barite precipitation during mixing with seawater (Discussion 4.4).

4.3. Barium isotopes in endmember vent fluids

Elemental compositions of endmember vent fluids are usually estimated by the interception of a regression line between elements and Mg or SO_4 concentrations at zero. This approach relies on the assumption that endmember vent fluid Mg or SO_4 is zero, and that any increase of Mg or SO_4 is due to seawater entrainment during sampling or subsurface mixing (e.g. Von Damm et al., 1985). However, it is difficult to use the same approach to determine the Ba compositions of endmember vent fluids due to barite precipitation during mixing with seawater. Even after the dregs correction, the corrected fluid Ba still shows non-conservative behavior (Fig. 3b), which implies that either some barite precipitation has occurred in subsurface prior to

venting of the fluids or that there is a low recovery of dregs in the samplers. Thus, we select the vent fluids with the highest Ba concentration (dregs corrected) from each hydrothermal vent field as the estimates of endmember vent fluids, except for EPR9-10°N which takes the average values of the three highest [Ba] samples. The endmember vent fluid [Ba] and $\delta^{138/134}$Ba values are summarized in Table 3 and Fig. 4.

Some difference in the endmember fluid Ba compositions can be found between ultramafic-hosted (Rainbow, MAR 36°N), basalt-hosted (EPR) and sediment-influenced (MEF) systems. The ultramafic-hosted endmember fluid (Rainbow) has the highest [Ba] and lowest $\delta^{138/134}$Ba values, although peridotite and serpentine, the most common source rocks in the ultramafic-hosted systems, have a much lower Ba concentration ([Ba]: 0.1-1.4 ppm, Andreani et al. 2014) than oceanic basalts ([Ba]: 3.9-160.3 ppm, Gale et al. 2013). This indicates that the endmember fluid [Ba] is not strongly correlated with the Ba contents of the source rocks in an ultramafic-hosted system. No reported $\delta^{138/134}$Ba data are available in peridotite and serpentine for direct comparison. The $\delta^{138/134}$Ba value of the basalt-hosted endmember fluids (EPR) is within the range of mid-ocean ridge basalt (MORB) $\delta^{138/134}$Ba values (+0.02 to +0.15‰) (Nielsen et al., 2018). The MEF vent fluid chemistry has shown the encounter with sediments during the fluid recharge zones, although MEF is not a sedimented MOR system (Lilley et al., 1993; Seyfried et al., 2003). The high $\delta^{138/134}$Ba value seen in the MEF endmember fluid may reflect the influence of sediments.

Overall, the endmember fluid $\delta^{138/134}$Ba values, ranging from -0.17 (± 0.07) to +0.09 (± 0.03) ‰, are within the range of $\delta^{138/134}$Ba values in their source rocks (MORBs and altered oceanic crust (AOC): -0.09 to +0.33‰, Nielsen et al., 2018;

374 pelagic sediments: -0.2 to +0.1 ‰, Crockford et al., 2019 and Bridgestock et al.,
375 2018) (Fig. 4b). As expected, water-rock interaction inside the hydrothermal system
376 appears to occur without Ba isotope fractionation, and a similar observation has been
377 discovered for Ca isotopes (Scheuermann et al., 2018). Therefore, source rocks may
378 be used to constrain the endmember vent fluid $\delta^{138/134}$Ba values.

379 Although the estimates of endmember vent-fluid Ba concentrations can be
380 affected by the uncertainty of Ba recovery in vent fluids, Ba isotopes may also
381 provide an approach to calculate the hypothetical concentration of the corrected Ba
382 ($[Ba]_{corr}$*) in vent fluids prior to barite precipitation and the recovery of Ba
383 (calculation details in supplementary material S2). The $\delta^{138/134}$Ba-derived hypothetical
384 $[Ba]_{corr}$* and [Mg] values can then be used to extrapolate the endmember fluid [Ba]
385 through a linear regression line at the intercept of zero Mg (Fig. 5). In general, the
386 correlations between the fluid [Ba] and [Mg] are improved when using the $[Ba]_{corr}$*
387 values. The extrapolated endmember fluid [Ba] values also agree with the highest
388 fluid $[Ba]_{corr}$ values observed in each vent field (Table 3), except for MEF (Fig. 5d).
389 In MEF, the $[Ba]_{corr}$* values correlate with the Ca and Cl concentrations in vent fluids
390 (Fig. S3). Vapor rich fluids with dissolved Cl contents below seawater are expected to
391 have low endmember Ba and Ca, because these species tend to partition into the
392 liquid phase in the region of liquid-vapor phase separation (Pester et al., 2015).

393 For future studies, Ba isotopes provide better constraints on the Ba
394 compositions in vent fluids if the endmember fluid $\delta^{138/134}$Ba compositions can be
395 provided. The endmember fluid $\delta^{138/134}$Ba values can be obtained by measuring fluid
396 samples with high Ba recovery and the source rocks for comparison.

397

398 **4.4. Barium isotope fractionation model: effective hydrothermal Ba input**

399 Hydrothermal input of dissolved Ba to the ocean is decreased by removal of
400 Ba due to barite precipitation during mixing between vent fluids and seawater. The
401 impact of this precipitation on Ba isotopes can be simply modelled using the known
402 fractionation during barite formation (e.g. von Allmen et al. 2010). This model can be
403 used to explain the variation of vent fluid $\delta^{138/134}$Ba values, and the expected isotope
404 composition of Ba after barite precipitation.

405 We apply a Rayleigh isotope fractionation model:

406 $$\delta^{138/134}Ba_{fluid} = \Delta^{138/134}Ba_{hyd\text{-}barite\text{-}fluid} \cdot \ln(f) + \delta^{138/134}Ba_{endmember} \quad (5)$$

407 where $\delta^{138/134}Ba_{endmember}$ and $\Delta^{138/134}Ba_{hyd\text{-}barite\text{-}fluid}$ denote the isotope composition of
408 the endmember fluids and hydrothermal barite isotope fractionation factor
409 ($\Delta^{138/134}Ba_{hyd\text{-}barite\text{-}fluid}$ = -0.35 ± 0.10 ‰), respectively; f is the fraction of dissolved Ba
410 remaining in the fluids (f = $[Ba]_{fluid}/[Ba]_{endmember}$). The endmember fluid [Ba] and
411 $\delta^{138/134}$Ba values from Table 3 are taken as the initial composition in each
412 hydrothermal vent field.

413 A Rayleigh fractionation model is appropriate in this situation, because the
414 precipitation of barite is rapid and the exchange between formed barite and dissolved
415 Ba is likely limited. A similar fractionation model has been demonstrated in other
416 isotopes (e.g. Ca and Zn) in hydrothermal systems (Amini et al., 2008; John et al.,
417 2008; Syverson et al. 2018).

418 Vent fluid Ba isotope data mostly fit within the trajectory of the isotope
419 fractionation model with a constant fractionation factor $\Delta^{138/134}Ba_{hyd\text{-}barite\text{-}fluid}$ = -0.35 ±
420 0.10 ‰ (Fig 5). This suggests that the Ba isotope variation in vent fluids is primarily
421 driven by barite precipitation and that the fractionation factor is relatively constant
422 between all the vent fields of this study. There are, however, a few samples that
423 cannot be explained by the fractionation model with the initial $\delta^{138/134}Ba_{endmember}$

424 compositions. These samples are mostly diffuse-flow type or have undergone
425 significant phase separation (Fig. 6). Such samples are likely to have differing initial
426 Ba compositions, and to reflect multiple Ba sources (e.g. non-basaltic Ba) and more
427 complex circulation environments. Ba diffusion may also introduce isotope
428 fractionation (van Zuilen et al., 2016).

429 The model can be used to calculate the Ba isotope compositions of the
430 effective hydrothermal component at the point of mixing where barite precipitation
431 stops ($\Omega_{barite} < 1$) and the remaining hydrothermal dissolved Ba starts to mix
432 conservatively with Ba in seawater. Barite saturation calculations, using a seawater
433 SO_4 concentration of 28 mmol/kg, indicate that fluids become undersaturated when
434 [Ba] < 0.2 μmol/kg. We extend the Rayleigh model to this value to assess the Ba
435 isotope compositions at the end point of hydrothermal plumes during mixing with
436 seawater (Fig. 6e-h). These end-point $\delta^{138/134}$Ba compositions, representing the
437 composition of dissolved Ba added to seawater, are high (+1.0 ~ +2.6 ‰), with an
438 average of +1.7 ± 0.7 ‰ (2SD).

439 In addition to barite precipitation, scavenging on to Fe oxyhydroxides and Mn
440 oxides may also remove Ba and cause isotope fractionation in hydrothermal plumes.
441 However, the fraction of Ba associated with the hydrothermal Fe oxyhydroxides is
442 relatively small in hydrothermal plumes (Feely et al. 1996). Barium scavenging onto
443 Fe oxyhydroxides or Mn oxides is likely to be a significantly less prominent process
444 in hydrothermal plumes, than incorporation into barite. Any isotope fractionation
445 associated with this process is unknown and would require future study to provide
446 further constraint.

447 Calculated end-point dissolved Ba compositions ($\delta^{138/134}$Ba = +1.7 ± 0.7 ‰)
448 are notably higher than the range observed in seawater (+0.22 ~ +0.65‰) (Fig. 4b).

449 Such an isotopically heavy Ba could explain the non-conservative mixing seen in
450 Atlantic deep waters (Hsieh and Henderson, 2017).
451
452 **4.5. Hydrothermal Ba isotopes and non-conservative mixing in deep waters**
453 To assess the influence of hydrothermal Ba input on the isotope composition
454 of Atlantic deep-waters, a three endmember mixing model is applied to these waters:
455 $f_{NADW} + f_{AABW} + f_{hyd} = 1$ (6)
456 $[Ba]_{sw} = f_{NADW}\,[Ba]_{NADW} + f_{AABW}\,[Ba]_{AABW} + f_{hyd}\,[Ba]_{hyd}$ (7)
457 $[Ba]_{sw}\cdot\delta^{138/134}Ba_{sw} = f_{NADW}\cdot[Ba]_{NADW}\cdot\delta^{138/134}Ba_{NADW} + f_{AABW}\cdot[Ba]_{AABW}\cdot\delta^{138/134}Ba_{AABW}$
458 $+ f_{hyd}\cdot[Ba]_{hyd}\cdot\delta^{138/134}Ba_{hyd}$ (8)
459 $F_{Ba\_hyd} = f_{hyd}\cdot[Ba]_{hyd}/[Ba]_{sw}$ (9)
460 where the subscripts identify the mixed deep seawater (sw) and each endmember:
461 NADW, AABW and the effective hydrothermal Ba (hyd); *f* denotes the relative
462 fractions of each endmember water, and F_{Ba_hyd} is the relative fraction of hydrothermal
463 Ba input in the Atlantic deep-waters.
464 The proximity of observed seawater compositions to these three end members
465 constrains the mixture of these components, as illustrated in Fig. 7. The calculated
466 fraction of hydrothermal plume water (f_{hyd}), the effective hydrothermal Ba
467 endmember, is 1.3 ~ 3.6 % in the deep water, taking into account the uncertainty of
468 endmember values. This assumes a combined two-stage water dilution factor of 1.4 ~
469 3.6 ($\times10^4$), firstly from vent fluids to the effective Ba endmember in the hydrothermal
470 plume and then to the deep water, assuming a maximum dilution in the first stage of ≈
471 500 (i.e. vent fluid [Ba] 100 μmol/kg / 0.2 μmol/kg). The dilution factor is of a
472 similar order of magnitude to the helium-3 dilution, 1.7 ~ 34 ($\times10^4$): from vent fluids
473 (endmember average ^{3}He: 17.1 pmol/kg, Jean-Baptiste et al., 2004) to deep waters

(^{3}He < 0.05 to 1 fmol/kg, Ruth et al., 2000 and Lupton, 1998). The calculated fraction of hydrothermal Ba input (F_{Ba_hyd}) consists of 3 ~ 9 % of the Ba in some Atlantic deep-waters. The deviations of seawater Ba isotopes from the conservative deep-water mixing can be explained by different degrees of hydrothermal Ba contributions in deep waters (Fig. 7b).

The hydrothermal input contributes isotopically heavy Ba to the ocean ($\delta^{138/134}$Ba = +1.7 ± 0.7 ‰) which, if a significant component of the ocean Ba cycle, would be hard to reconcile with a balanced Ba isotope budget. Riverine Ba is the main Ba input to the ocean with a range of measured isotope values from -0.06 to +0.46‰). The major Ba output is biogenetic barite and its burial in marine sediments which has a $\delta^{138/134}$Ba value from -0.21 to +0.11‰. This range overlaps that of rivers (Fig. 4b) but may be somewhat lower on average, so that observed inputs may be isotopically heavier than outputs. The heavy input from hydrothermal Ba implies that either (1) hydrothermal Ba flux is small; or (2) other isotopically heavy sinks are missing. The total global hydrothermal Ba vent flux has been estimated to be 2.40 to 3.35 Gmol/yr (Paytan and Kastner, 1996; Dickens et al., 2003), based on the end-member vent fluid [Ba] prior to barite precipitation (i.e. with Ba concentration > 10 μmol/kg, Von Damm et al., 1985). This flux is about 4 ~ 6 times smaller than the riverine Ba flux (14.75 Gmol/yr, Wolgemuth and Broecker, 1970; Dickens et al., 2003). Considering that hydrothermal [Ba], after precipitation of barite, is 0.2 μmol/kg, the effective hydrothermal Ba flux to the global ocean will be much smaller than the initial vent flux. More precise assessments of Ba fluxes and isotopic compositions in other sources (e.g. cold seeps and submarine groundwater discharge) and sinks (e.g. Fe-Mn oxides and oxyhydroxides) are needed to fully constrain the Ba isotope budget in the ocean.

Seawater SO_4 plays an important role in barite saturation and hence in determining the influence of hydrothermal Ba input and its non-conservative behavior in the ocean. In an ocean with lower SO_4 concentration than the modern ocean, barite precipitation during mixing would cease at a higher Ba concentration, and consequently lower $\delta^{138/134}$Ba value (Fig. 8). Reconstructions of marine sulfur isotope values suggest that seawater SO_4 concentration may have varied from present levels to much lower concentrations of only a few mmol/kg during the Phanerozoic (Canfield and Farquhar, 2009; Turchyn and DePaolo, 2019). These changes could have a large impact on the hydrothermal Ba inputs to the ocean. Deep sea corals (Hemsing et al., 2017; Geyman et al., 2019) and hydrothermal barites (Crockford et al., 2019) can potentially be used to reconstruct water and hydrothermal Ba isotope compositions in the past. The relationship between seawater SO_4 and barite precipitation may allow Ba and Ba isotopes to serve as a tracer to reveal the history of MOR hydrothermal Ba inputs and seawater SO_4 in the ocean.

5. Conclusions

We present the first Ba isotope data in MOR hydrothermal vent fluids from numerous hydrothermal systems, including basalt-hosted, ultramafic-hosted and sediment-influenced hydrothermal systems. The vent fluids display a wide range of dissolved Ba concentrations and are generally supersaturated with respect to barite ($\Omega_{barite} > 1$). The endmember vent fluid $\delta^{138/134}$Ba values, ranging from -0.17 to +0.09 ‰, agree with the values observed in source rocks, which implies that water-rock interaction has a limited effect on the Ba isotope variation in vent fluids. Barite precipitation removes isotopically light Ba from vent fluids during the mixing between Ba-bearing vent fluids and SO_4-bearing seawater. This mixing follows a

Rayleigh fractionation with a fractionation factor of $\Delta^{138/134}Ba_{hyd\text{-}barite\text{-}fluid}$ = -0.35 ± 0.10 ‰. Barite precipitation controls the magnitude and composition of hydrothermal Ba input ultimately added as dissolved Ba to seawater. The effective hydrothermal Ba composition is calculated as $[Ba]_{hyd}$ = 0.2 μmol/kg and $\delta^{138/134}Ba_{hyd}$ = +1.7 ± 0.7 ‰. Such an isotopically heavy Ba can explain the non-conservative mixing seen in deep waters, with hydrothermal input around 3 ~ 9 % of the Ba in some Atlantic deep waters. The relationship between vent fluid Ba and seawater SO_4 makes Ba isotopes a potential tracer to reconstruct the history of MOR hydrothermal Ba inputs and seawater SO_4 concentrations in the past.

Acknowledgements

We thank Phil Holdship for his assistance with the Quad-ICP-MS analysis. We would also like to thank John Higgins for discussion. Moreover, we wish to thank the captain and crew of UNOLS ships and support vehicles (U.S.) for their assistance in planning and execution, without which the vent fluid samples reported here would not have been possible. Vent fluid sampling studies conducted by University of Minnesota researchers benefited as well from efforts of students and staff scientists. These field and related experimental studies were supported through US NSF grants: 0549547, 0751771, 0813861, 0961188 and 1736679 (WES). The Associate Editor and three anonymous reviewers are appreciated for their valuable comments to improve this paper.

References

Amini M., Eisenhauer, A., Böhm, F., Fietzke, J., Bach, W., Garbe-Schönberg, D., Rosner, M., Bock, B., Lackschewitz, K. S. and Hauff, F. (2008) Calcium isotope ($\delta^{44/40}Ca$) fractionation along hydrothermal pathways, Logatchev field (Mid-Atlantic Ridge, 14°45'N). *Geochimica et Cosmochimica Acta* **72**, 4107–4122.

552 Andreani, M., Escartin, J., Delacour, A., Ildefonse, B., Godard, M., Dyment, J.,
553 Fallick, A. E. and Fouquet Y. (2014) Tectonic structure, lithology, and hydrothermal
554 signature of the Rainbow massif (Mid-Atlantic Ridge 36°14'N). Geochemistry,
555 Geophysics, Geosystems **15**, 3543–3571.
556
557 Bates S. L., Hendry, K. R., Pryer, H. V., Kinsley, C. K., Pyle, K. M., Woodward, E.
558 M. and Horner, T. J. (2017) Barium isotopes reveal role of ocean circulation on
559 barium cycling in the Atlantic. *Geochimica et Cosmochimica Acta* **204**, 286-299.
560
561 Bemis, K., Lowell, R. P. and Farough., A. (2012) Diffuse flow on and around
562 hydrothermal vents at mid-ocean ridges. *Oceanography* **25**, 182–191.
563
564 Bishop, J. K. B. (1998) The barite-opal-organic carbon association in oceanic
565 particulate matter. *Nature* **332**, 341-343.
566
567 Blount, C. W. (1977) Barite solubilities and thermodynamic quantities up to 300oC
568 and 1400 bars. *American Mineralogist* **62**, 942-957.
569
570 Böttcher M. E, Neubert, N., von Allmen, K., Samankassou, E. and Nagler, T. F.
571 (2018) Barium isotope fractionation during the experimental transformation of
572 aragonite to whiterite and of gypsum to barite, and the effect of ion (de)solvation.
573 *Isotopes in Environmental and Health Studies* **54**, 324-335.
574
575 Bridgestock, L., Hsieh, Y-T., Porcelli, D., Homoky, W. B., Bryan, A. and Henderson,
576 G. M. (2018) Controls on the barium isotope compositions of marine sediments.
577 *Earth and Planetary Science Letters* **481**, 101-110.
578
579 Butterfield, D. A., Massoth, G. J., McDuff, R. E., Lupton, J. E. and Lilley, M. D.
580 (1990) Geochemistry of hydrothermal fluids from Axial Seamount hydrothermal
581 emissions study vent field, Juan de Fuca Ridge: Subseafloor boiling and subsequent
582 fluid-rock interaction. *Journal of Geophysical Research* **95**, 12895-12921.
583
584 Butterfield, D. A., McDuff, R. E., Mottl, M. J., Lilley, M. D., Lupton, J. E.
585 and Massoth, G. J. (1994) Gradients in the composition of hydrothermal fluids from
586 the Endeavor segment vent field: Phase separation and brine loss, *Journal of*
587 *Geophysical Research* **99**, 9561–9583.
588
589 Butterfield, D. A. and Massoth, G. J. (1994) Geochemistry of north Cleft segment
590 vent fluids: temporal changes in chlorinity and their possible relation to recent
591 volcanism. *Journal of Geophysical Research* **99**, 4951-4968.
592
593 Campbell, A. C., Palmer, M. R., Klinkhammer, G. P., Bowers, T. S., Edmond, J. M.,
594 Lawrence, J. R., Casey, J. F., Thompson, G., Humphris, S., Rona, P. and Karson, J. A.
595 (1988) The chemistry of hot springs on the Mid-Atlantic Ridge. *Nature* **335**, 514–519.
596
597 Canfield, D. E., and Farquhar, J. (2009) Animal evolution, bioturbation, and the
598 sulfate concentration of the oceans. Proceedings of the National Academy of Sciences
599 of the United States of America 106, 8123-8127.
600

Cao, Z., Siebert., C., Hathorne, E. C., Dai, M. and Frank, M. (2020) Corrigendum to "Constraining the oceanic barium cycle with table barium isotopes" [Earth Planet. Sci. Lett. 434 (2016) 1-9]. *Earth and Planetary Science Letters* 530, 116003.

Cao, Z., Sibert, C., Hathorne, E. C., Dai, M. and Frank, M. (2016) Constraining the oceanic barium cycle with table barium isotopes. *Earth and Planetary Science Letters* 434, 1-9.

Charlou, J. L., Fouquet, Y., Donval, J. P., Auzende, J. M., Jean-Baptiste, P., Stievenard, M. and Michel, S. (1996) Mineral and gas geochemistry of hydrothermal fluids on an ultrafast spreading ridge: East Pacific Rise, 17^{o} to 19^{o}S (Naudur cruise, 1993) - phase separation processes controlled by volcanic and tectonic activity. *Journal of Geophysical Research* **101**, 15899-15919.

Charlou, J. L., Donval, J. P., Fouquet, Y., Jean-Baptiste, P. and Holm, N. (2002) Geochemistry of high H2 and CH4 vent fluids issuing from ultramafic rocks at the Rainbow hydrothermal field (36^{o}14'N, MAR). *Chemical Geology* **191**, 345–359.

Church, T. M. and Wolgemuth, K. (1972) Marine barite saturation. *Earth and Planetary Science Letters* 15, 35-44.

Coogan, L. A., Seyfried, W. E., Jr., and Pester, N. J. (2019) Environmental controls on mid-ocean ridge hydrothermal fluxes. *Chemical Geology* **528**, 119285.

Crockford, P. W., Wing, B. A., Paytan, A., Hodgskiss, M. S. W., Mayfield, K. K., Hayles, J. A., Middleton, J. E., Ahn, A-S. C., Johnson, D. T., Caxito, F., Uhlein, G., Halverson, G. P., Eickmann, B., Torres, M. and Horner, T. J. (2019) Barium-isotopic constraints on the origin of post-Marinoan barites. *Earth and Planetary Science* **519**, 234-244.

Dickens, G. R., Fewless, T., Thomas, E. and Bralower T. J. (2003) Excess barite accumulation during the Paleocene-Eocene Thermal Maximum: Massive input of dissolved barium from seafloor gas hydrate reservoirs, *in* Ginerich, P. et al., eds., Causes and consequences of globally warm climates in the early Paleogene: Geological Society of America Special Paper **369**, 11-23.

Douville, E., Charlou, J. L., Oelkers, E. H., Bienvenu, P., Jove Colon, C. F., Donval, J. P., Fouquet, Y., Prieur, D. and Appriou, P. (2002) The Rainbow vent fluids (36^{o}14'N,MAR): the influence of ultramafic rocks and phase separation on trace metal content in Mid-Atlantic Ridge hydrothermal fluids. *Chemical Geology* **184**, 37–48.

Elderfield, H. and Schultz, A. (1996) Mid-ocean ridge hydrothermal fluxes and the chemical composition of the ocean. *Annual Reviews of Earth and Planetary Sciences* **24**, 191-224.

Feely, R. A., Baker, E. T., Marumo, K., Urabe, T., Ishibashi, J., Gendron, J., Lebon, G. T., Okamura, K. (1996) Hydrothermal plume particles and dissolved phosphate over the susperfast-spreading southern East Pacific Rise. *Geochimica et Cosmochimica Acta* **60**, 2297-2323.

Fornari, D. J., Von Damm, K. L., Bryce, J. G., Cowen, J. P., Ferrini, V., Fundis, A., Lilley, M. D., Luther III, G. W., Mullineaux, L. S., Perfit, M. R., Meana-Prado, M. F., Rubin, K. H., Seyfried Jr., W. E., Shank, T. M., Soule, S. A., Tolstoy, M. and White, S. M. (2012) The East Pacific Rise between 9°N and 10°N: Twenty-five years of integrated, multidisciplinary oceanic spreading center studies. *Oceanography* **25**,18–43.

Foustoukos, D. I. and Seyfried, W.E., Jr. (2007) Quartz solubility in the two-phase and critical region of the NaCl-KCl-H_2O system: Implications for submarine hydrothermal vent systems at 9°50'N East Pacific Rise. *Geochimica et Cosmochimica Acta* **71**, 186-201.

Foustoukos, D. I., Pester, N. J., Ding, K. and Seyfried, W. E. (2009) Dissolved carbon species in associated diffuse and focused flow hydrothermal vents at the Main Endeavour Field, Juan de Fuca Ridge: phase equilibria and kinetic constraints. *Geochemistry, Geophysics, Geosystems* **10**, Q10003

Gale, A., Dalton, C. A., Langmuir, C. H., Su, Y. and Schilling J.-G (2013) The mean composition of ocean ridge basalts. *Geochemistry, Geophysics, Geosystems* **14**, 489-518.

Gartman, A., Findlay, A. J., Hannington, M., Garbe-Schonbert, D., Jamieson, J. W. and Kwasnitschka T. (2019) The role of nanoparticles in mediating element deposition and transport at hydrothermal vents. *Geochimica et Cosmochimica Acta* **261**, 113-131.

Gartman, A., Hannington, M., Jamieson, J. W., Peterkin, B., Garbe-Schonberg, D., Findlay, A. J., Fuchs, S. and Kwasnitschka, T. (2018) Boiling-induced formation of colloidal gold in black smoker hydrothermal fluids. *Geology* **46**, 39-42.

Gartman, A., Findlay, A. J. and Luther, G. W. (2014) Nanoparticulate pyrite and other nanoparticles are a widespread component of hydrothermal vent black smoker emissions. *Chemical Geology* **366**, 32-41.

German, C. and Von Damm, K. (2003) Hydrothermal processes. H. Elderfield (Ed.), Treatise on Geochemistry: The Oceans and Marine Geochemistry, Elsevier/Pergamon, Oxford, pp. 181-222.

German, C. and Seyfried, W.E., Jr. (2014) Hydrothermal Processes. The Oceans & Marine Geochemistry. Treatise on Geochemistry Series, vol. 8. Pp. 191-233.

Geyman, B. M., Ptacek, J. L., LaVigne, M., and Horner, T. J. (2019) Barium in deep-sea bamboo corals: Phase associations, barium stable isotopes, & prospects for paleoceanography. *Earth and Planetary Science Letters* **525**, 115751.

Gou, L., Jon, Z., Galy, A., Gong, Y., Nan, C. J., Wnag, X., Bouchez, J., Cai, H., Chen, J., Yu, H. and Huang, F. (2020) Seasonal riverine barium isotopic variation in the middle Yellow River: Sources and Fractionation. *Earth and Planetary Science Letters* **531**, 115990.

Hanor, J. S. (2000) Barite-celestine geochemistry and environments of formation. C.N. Alpers, J.L. Jambor, D.K. Nordstrom (Eds.), *Reviews in Mineralogy & Geochemistry – Sulfate Minerals*, Vol. 40, Mineralogical Society of America, Washington, D.C., pp. 193-275

Hemsing, F., Hsieh Y-T., Bridgestock, L., Spooner, P. T., Robinson, L., F., Frank, N. and Henderson, G. M. (2018) Barium isotopes in cold-water corals. *Earth and Planetary Science Letters* **491**, 183-192.

Horner, T. J., Kinsley, C. W. and Nielsen, S. G. (2015) Barium-isotopic fractionation in seawater mediated by barite cycling and oceanic circulation. *Earth and Planetary Science Letters* **430**, 511-522.

Horner, T. J., Pryer, H. V., Nielsen, S. G., Crockford, P. W., Gauglitz, J. M., Wing, B. A. and Ricketts, R. D. (2017) Pelagic barite precipitation at micromolar ambient sulfate. *Nature Communications* **8**, 1242.

Hsieh, Y-T. and Henderson, G. M. (2017) Barium stable isotopes in the global ocean: Tracer of Ba inputs and utilization. *Earth and Planetary Science Letters* **473**, 269-278.

James, R. H., Green, D. R. H., Stock, M. J., Alker, B. J., Banerjee, N. R., Cole, C., German, C. R., Huvenne, V. A. I., Powell, A. M. and Connelly, D. P. (2014) Composition of hydrothermal fluids and mineralogy of associated chimney material on the East Scotia Ridge back-arc spreading centre. *Geochimica et Cosmochimica Acta* **139**, 47-71.

Jamieson, W. D., Hannington M. D., Tivey, M. K., Hansteen, T., Williamson, N. M. B., Steward, M., Fietzke, J., Butterfield, D., Frische, M., Allen, L., Cousens, B. and Langer, J., (2016) Precipitation and growth of barite within hydrothermal vent deposits from the Endeavour Segment, Juan de Fuca Ridge. *Geochimica et Cosmochimica Acta* **173**, 64-85.

Jean-Baptiste, P., Fourre, E., Charlou, J. L., German, C. R. and Radford-Knoery, J. (2004) Helium isotopes at the Rainbow hydrothermal site (Mid-Atlantic Ridge, 36°14'N). *Earth and Planetary Science Letters* **221**, 325-335.

John, S., Rouxel, O., Craddock, P., Engwall, A., Boyle E. (2008) Zinc stable isotopes in seafloor hydrothermal vent fluids and chimneys. *Earth and Planetary Science Letters* **269**, 17-28.

Koski, R. A., Jonasson, I. R., Kadko, D. C., Smith, V. K., and Wong, F. L. (1994) Compositions, growth mechanisms, and temporal relations of hydrothermal sulfide-sulfate-silica chimneys at the northern Cleft Segment, Juna de Fuca Ridge, *Journal of Geophysical Research Solid Earth* **99**, 4813-4832.

Kumagai, H., Nakamura, K., Toki, T., Morishita, T., Okino, K., Ishibashi, J. I., Tsunogai, U., Kawagucci, S., Gamo, T., Shibuya, T., Sawaguchi, T., Neo, N., Joshima, M., Sato, T. and Takai, K. (2008) Geological background of the Kairei and

751 Edmond hydrothermal fields along the Central Indian Ridge: implications of their
752 vent fluids' distinct chemistry *Geofluids* **8**, 239-251.
753
754 Li, Y.-H. and Schoomaker, J.E. (2003) Chemical composition and mineralogy of
755 marine sediments. *Treatise on Geochemistry* **7**, 1-35.
756
757 Lilley, M. D., Butterfield, D. A., Olson, E. J., Lupton, J. E., Macko, S. A.
758 and McDuff, R.E. (1993) Anomalous CH4 and NH4+ concentrations at an
759 unsedimented mid-ocean-ridge hydrothermal system. *Nature* **364**, 45-47.
760
761 Lupton, J. (1998) Hydrothermal helium plumes in the Pacific Ocean. *Journal of*
762 *Geophysical Research* **103**, 15853-15868.
763
764 Martinez-Ruiz, F., Jroundi, F., Paytan, A., Guerra-Tschuschke, I., Abad, M. M., and
765 Gonzalez-Munoz, M. T. (2018) Barium bioaccumulation by bacterial biofilms and
766 implications for Ba cycling and use of Ba proxies. *Nature Communications* **9**, 1619.
767
768 Metz, S. and Trefry, J. H. (2000) Chemical and mineralogical influences on
769 concentrations of trace metals in hydrothermal fluids. *Geochimica et Cosmochimica*
770 *Acta* **64**, 2267-2279.
771
772 Monnin, C. and Galinier C. (1988) The solubility of celestite and barite in electrolyte
773 solutions and natural waters at 25°C: A thermodynamic study. *Chemical Geology* **71**,
774 283-296.
775
776 Monnin, C. (1999) A thermodynamic model for the solubility of barite and celestite in
777 electrolyte solutions and seawater from 0 to 200^{o}C and to 1 kbar. *Chemical Geology*
778 **153**, 187–209.
779
780 Monnin, C., Jeandel, C., Cattaldo, T. and Dehairs, F. (1999) The marine barite
781 saturation state of the world's oceans. *Marine Chemistry* **65**, 253-261.
782
783 Monnin, C., Wheat C. G, Dupre B., Elderfield H. and Mottl M. M. (2001) Barium
784 geochemistry in sediment porewaters and formation waters of the oceanic crust on
785 eastern flank of the Juan de Fuca ridge (ODP Leg 168). *Geochemistry, Geophysics,*
786 *Geosystems*, 2000GC000073.
787
788 Nan, X-Y, Yu, H-M., Rudnick, R. L., Gaschnig, R. M., Xu, J., Li, W-Y., Zhang, Q.,
789 Jin, Z-D, Li, X-H. and Huang, F. (2018) Barium isotopic composition of the upper
790 continental crust. *Geochimica et Cosmochimica Acta* **233**, 33-49.
791
792 Nielsen, S. G., Horner, T. J., Pryer, H. V., Blusztajn, J., Shu, Y., Kurz, M. D. and Le
793 Roux, V. (2018) Barium isotope evidence for pervasive sediment recycling in the
794 upper mantle. *Science Advances* **4**, eaas8675
795
796 Nielsen, S. G., Shu, Y., Auro, M., Yogodzinski, G., Shinjo, R, Plank, T., Kay, S. M.
797 and Horner, T. J. (2020) Barium isotope systematics of subduction zones. *Geochimica*
798 *et Cosmochimica Acta* **275**, 1-18.
799

Paytan, A and Kastner, M. (1996) Benthic Ba fluxes in the central Equatorial Pacific, implications for the oceanic Ba cycle, *Earth and Planetary Science Letters* **142**, 439-450

Pester, N. J., Rough, M., Ding, K., Seyfried, W. E., Jr. (2011) A new Fe/Mn geothermometer for hydrothermal systems: implications for high-salinity fluids at 13 N on the East Pacific Rise. *Geochimica et Cosmochimica Acta* **75**, 7881-7892.

Pester, N. J., Ding, K. and Seyfried, W. E., Jr. (2014) Magmatic eruptions and iron volatility in deep-sea hydrothermal fluids. *Geology* **42**, 255-258.

Pester, N. J., Ding, K. and Seyfried, W. E. Jr. (2015) Vapor–liquid partitioning of alkaline earth and transition metals in NaCl-dominated hydrothermal fluids: An experimental study from 360 to 465°C, near-critical to halite saturated conditions. *Geochimica et Cosmochimica Acta* **168**, 111-132.

Ruth, C., Well, R. and Roether, W. (2000) Primordial 3He in South Atlantic deep waters from sources on the Mid-Atlantic Ridge. *Deep Sea Research Part I* **47**, 1059-1075.

Rouxel, O., Shanks, W. C., Bach, W. and Edwards, K. J. (2008) Integrated Fe- and S-isotope study of seafloor hydrothermal vents at East Pacific rise 9-10°N. *Chemical Geology* **252**, 214-227.

Scheuermann, P. P., Syverson, D. D., Higgins, J. A., Pester, N. J. and Seyfried, W. E., Jr. (2018) Calcium isotope systematic at hydrothermal conditions: Mid-ocean ridge vent fluids and experiments in the $CaCO_4$-NaCl-H_2O system. *Geochimica et Cosmochimica Acta* **226**, 18-35.

Seewald, J. S., Doherty, K. W., Hammar, T. R. and Liberatore, S. P. (2002) A new gas-tight isobaric sampler for hydrothermal fluids. *Deep Sea Research Part I: Oceanographic Research Papers* **49**, 189-196.

Seyfried, W. E., Jr., Ding, K. and Berndt. M. E. (1991) Phase equilibria constraints on the chemistry of hot spring fluids at mid-ocean ridges. *Geochimica et Cosmochimica Acta* **55**, 3559-3580.

Seyfried, W. E., Jr., Seewald, J. S., Berndt, M. E., Ding, K. and Foustoukos D. I. (2003) Chemistry of hydrothermal vent fluids from the Main Endeavour Field, northern Juan de Fuca Ridge: Geochemical controls in the aftermath of June 1999 seismic events. *Journal of Geophysical Research: Solid Earth* **108**, 1-23.

Seyfried, W. E., Jr., Pester, N. J., Ding, K. and Rough, M. (2011) Vent fluid chemistry of the Rainbow hydrothermal system (36^{o}N, MAR): Phase equilibria and in situ pH controls on subseafloor alteration processes. *Geochimica et Cosmochimica Acta* **75**, 1574-1593.

Shikazono, N., (1994) Precipitation mechanisms of barite in sulfate-sulfide deposits in back-arc basins. *Geochimica et Cosmochimica Acta* **58**, 2203-2213.

Syverson, D. D., Luhmann, A. J., Tan, C. Y., Borrok, D. M., Ding, K. and Seyfried, W. E., Jr. (2017) Fe isotope fractionation between chalcopyrite and dissolved Fe during hydrothermal recrystallization: An experimental study at 350 degrees C and 500 bars. *Geochimica et Cosmochimica Acta* **200**, 87-109.

Syverson, D. D., Scheuermann, P., Higgins, J. A., Pester, N. J., Seyfried, W. E., Jr. (2018) Experimental partitioning of Ca isotopes and Sr into anhydrite: Consequences for the cycling of Ca and Sr in subseafloor mid-ocean ridge hydrothermal systems. *Geochimica et Cosmochimica Acta* **236**, 160-178.

Tivey, M. K. (2007) Generation of seafloor hydrothermal vent fluids and associated mineral deposits. *Oceanography* **20**, 50-65.

Turchyn, A. V. and DePaolo, D. J. (2019) Seawater chemistry through Phanerozoic time. *Annual Reviews of Earth and Planetary Sciences* **47**, 197-224.

van Zuilen, K., Muller, T., Nagler, T. F., Dietzel, M. and Kusters, T. (2016) Experimental determination of barium isotope fractionation during diffusion and adsorption processes at low temperatures. *Geochimica et Cosmochimica Acta* **186**, 226-241.

von Allmen, K., Bottcher, M. E., Samankassou, E. and Nagler, T. F. (2010) Barium isotope fractionation in the global barium cycle: First evidence from barium minerals and precipitation experiments. *Chemical Geology* **277**, 70-77.

Von Damm, K. L., Edmond, J. M., Grant, B., Measures, C. I., Walden, B. and Weiss, R. F. (1985) Chemistry of submarine hydrothermal solutions at 21°N, East Pacific Rise. *Geochimica et Cosmochimica Acta* **49**, 2191-2220.

Von Damm, K. L. (1990) Seafloor hydrothermal activity – Black smoker chemistry and chimneys. *Annual Reviews of Earth and Planetary Sciences* **18**, 173-204.

Von Damm, K. L., Oosting, S. E., Kozlowski, R., Buttermore, L. G., Colodner, D., Edmonds, H. N., Edmond, J. M. and Grebmeir, J. M. (1995) Evolution of East Pacific Rise hydrothermal vent fluids following a volcanic eruption. *Nature* **375**, 47– 50.

Von Damm, K. L. (2000) Chemistry of hydrothermal vent fluids from 9^{o}-10^{o}N, East Pacific Rise: "Time zero," the immediate posteruptive period. *Journal of Geophysical Research* **105**, 11203-11222.

Von Damm, K. L., Lilley, M. D., Shanks III, W. C., Brockington, M., Bray, A. M., O'Grady, K. M., Olson, E., Graham, A., Proskurowski, G. and the SouEPR Science Party (2003) Extraordinary phase separation and segregation in vent fluids from the southern East Pacific Rise. *Earth and Planetary Science Letters* **206**, 365-378.

Wolgemuth, K., and Broecker, W. S. (1970) Barium in sea water, *Earth and Planetary Science Letters* **8**, 372-378.

Wu, S.-J., Yang, C.-J., Ding, K. and Tan, C. (2015) A remotely operated serial sampler for collecting gas-tight fluid samples. *China Ocean Engineering* **29**, 783-792.

Yucel, M., Gartman, A., Chan, C. S. and Luther, G. W. (2011) Hydrothermal vents as a kinetically stable source of iron-sulphide-bearing nanoparticles to the ocean. *Nature Geoscience* **4**, 367-371.

Table and figure captions

Table 1 Vent fluid and particle (dregs) sample information, temperature, Mg, SO_4 and Ba concentrations and Ba isotope compositions.

Table 2 Vent fluid and particle (dregs) Ba concentration, isotope composition and fractionation factor.

Table 3 Summary of calculated Ba compositions in endmember fluids.

Figure 1. Compilations of seawater [Ba] and $\delta^{138/134}$Ba data below 2000 m in the Atlantic and Southern Oceans. Deep-water $\delta^{138/134}$Ba and [Ba] data in the South Atlantic (2000~3000 m) show deviations (~ 0.1 ‰ $\delta^{138/134}$Ba offsets), highlighted by the yellow arrow and circle, from the conservative mixing line (the dashed line and grey band ±2σ) between NADW and AABW during the N-S Atlantic water transport. Additional Ba inputs (e.g. hydrothermal input) may be responsible for the non-conservative behavior. The Ba compositions of NADW ([Ba] ≈ 51 nmol/kg; $\delta^{138/134}$Ba ≈ +0.45‰) and AABW ([Ba] ≈ 103 nmol/kg; $\delta^{138/134}$Ba ≈ +0.25‰) have been assessed by Hsieh and Henderson (2017) and Bates et al. (2017). Compiled data are from Horner et al. (2015), Bates et al. (2017), Hsieh and Henderson (2017), Bridgestock et al. (2018) and Hemsing et al., (2018).

Figure 2. Location of MOR hydrothermal vent fields and sampling years in this study.

927 **Figure 3.** Ba, Mg and SO_4 concentrations and Ba isotope compositions for MOR
928 hydrothermal vent fluids from MAR (Rainbow 36^{o}N and TAG26^{o}N), EPR (9-10^{o}N
929 and 13^{o}N) and JdFR (MEF and ASHES) vent systems. **(a)** Hydrothermal vent fluid
930 [SO_4] versus [Mg] (dashed line represents conservative mixing between vent fluids
931 and seawater). **(b)** Plot of vent fluid [Ba] versus [SO_4], and the expected curve for
932 barite saturation (Ω_{barite} = 1) at deep-water T-P condition (1^{o}C and 500bar),
933 demonstrating that many samples are super-saturated for barite. The circles show the
934 focused-flow fluids and the triangles show the diffuse-flow samples. The closed
935 symbols show the dregs corrected fluid Ba compositions (equation 1) and the open
936 symbols show all the non-corrected data. Seawater and vent fluid conservative mixing
937 is illustrated in dashed lines. Removal of Ba by barite precipitation during mixing
938 with seawater is highlighted by the purple arrow. **(c)** Plot of Ba isotopes and Ba/Mg
939 ratios for vent fluids (both dregs corrected and non-corrected, Section 4.2) indicating
940 Ba isotope fractionation during removal in vent fluids. The data show the largest
941 range of $\delta^{138/134}$Ba (-0.26 ~ +0.91 ‰) so far seen in marine environments. Seawater
942 Ba concentration and isotope data are the average values (between 2000 and 3000m)
943 from the North Atlantic (BATS, Hsieh and Henderson, 2017) and North Pacific
944 (SAFe, Geyman et al., 2019).
945
946 **Figure 4. (a)** Comparisons of vent fluid $\delta^{138/134}$Ba values between different vent
947 fields. The open red diamonds are the measured values and the solid red diamonds are
948 the dregs corrected values. The black squares are the estimates of endmember vent
949 fluid in each field. **(b)** Comparisons of $\delta^{138/134}$Ba values in marine systems: seawater
950 (Horner et al., 2015; Hsieh and Henderson, 2017; Bates et al., 2017; Horner et al.,
951 2017; Bridgestock et al., 2018; Hemsing et al., 2018; Geyman et al., 2019; Cao et al.,

952 2020), rivers (Cao et al., 2016; Hsieh and Henderson, 2017; Gou et al., 2020),
953 MORBs and AOC (Nielsen et al., 2018; Nielsen et al., 2020), pelagic sediments
954 (Bridgestock et al., 2018; Crockford et al., 2019; Nielsen et al., 2020), and
955 hydrothermal vent fluids (this study). The hydrothermal vent fluid data show the
956 largest range of $\delta^{138/134}$Ba (-0.26 ~ +0.91 ‰) so far seen in marine environments. The
957 effective hydrothermal input $\delta^{138/134}$Ba (+1.7 ± 0.7‰, red square) is extrapolated by
958 barite saturation and Ba isotope fractionation models (Discussion 4.4).
959
960 **Figure 5.** Barium versus magnesium in the (a) Rainbow, (b) MEF, (c) EPR9-10^{o}N,
961 and (d) EPR13^{o}N hydrothermal vent fluids. The blue open circles show the dregs
962 corrected Ba concentrations ($[Ba]_{corr}$) and the red closed circles show the $\delta^{138/134}$Ba-
963 derived hypothetical Ba concentration ($[Ba]_{corr}$*) prior to barite precipitation. The
964 dashed lines show the linear regressions through the [Ba] and [Mg] data, which are
965 used to extrapolate the endmember fluid [Ba] at the intercept of zero Mg (±1SD).
966
967 **Figure 6.** Ba isotopes and concentrations in the Rainbow, EPR9-10^{o}N, EPR13^{o}N and
968 MEF hydrothermal vent fluids with seawater mixing, Rayleigh fractionation and
969 barite saturation models. **(a-d)** The data of Ba isotopes and 1/[Ba] show increased
970 $\delta^{138/134}$Ba as [Ba] in vent fluids decreases. A Rayleigh fractionation model with a
971 fractionation factor $\Delta^{138/134}Ba_{hyd\text{-}barite\text{-}fluid}$ = -0.35 ± 0.10 ‰ (orange and blue lines) is
972 applied to fit the data. The initial endmember fluid compositions are taken from Table
973 3. The closed and open circles are the dregs corrected and uncorrected fluid Ba
974 compositions respectively. Samples outside the range of the model trajectory are
975 labeled individually. They are likely to be affected by phase separation (PS),
976 evidenced by low [Cl] and [Ca] (Table S1), or diffuse-flow (DF) in a more complex

977 circulation environment. Foustoukos et al. (2009) have also noticed that Smoke &
978 Mirrors (S&M) may have a different circulation environment from other focused-flow
979 vents in the MEF vent field. **(e-h)** Extrapolation of curves in (a-d) to the [Ba] values
980 at the end point of hydrothermal plumes during mixing with seawater. Barite
981 saturation values ($\Omega_{barite} = 1$) are shown by green vertical lines. Once [Ba] becomes
982 under-saturated (< 0.2 μmol/kg, $\Omega_{barite} < 1$), remaining Ba in the plumes starts to mix
983 conservatively with seawater, as indicated by the black arrow. The effective
984 hydrothermal Ba isotope compositions are labeled in green. Seawater Ba data are
985 from Hsieh and Henderson (2017) and Geyman et al. (2019). NA and NP stand for the
986 North Atlantic and the North Pacific seawaters respectively. The brown bends refer to
987 the range of $\delta^{138/134}$Ba values in MORBs (+0.02 to +0.15‰; Nielsen et al., 2018).
988
989 **Figure 7.** Estimated hydrothermal Ba input in the deep Atlantic Ocean. **(a)** Three
990 endmembers mixing model. The red square shows the hydrothermal value with its
991 uncertainty ([Ba] ≈ 200 nmol/kg; $\delta^{138/134}$Ba = +1.7 ± 0.7‰), and the blue and green
992 squares show the compositions of NADW ([Ba] ≈ 51 nmol/kg; $\delta^{138/134}$Ba ≈ +0.45‰)
993 and AABW ([Ba] ≈ 103 nmol/kg; $\delta^{138/134}$Ba ≈ +0.25‰) respectively (Hsieh and
994 Henderson, 2017; Bates et al., 2017). The yellow square shows the mixed seawater
995 composition (SW_{SA}) between 2000 ~ 3000 m depth from the South Atlantic ([Ba] ≈
996 78 nmol/kg; $\delta^{138/134}$Ba ≈ +0.39‰) (Horner et al., 2015; Hsieh and Henderson, 2017).
997 Dashed mixing lines between the hydrothermal Ba and deep water endmembers are
998 labeled with open circles to indicate the fractions of hydrothermal Ba input (F_{Ba_hyd})
999 in the deep water Ba (0-100%). The non-hydrothermal Ba fractions between NADW
1000 and AABW are labeled with crosses. As the uncertainty of the hydrothermal $\delta^{138/134}$Ba
1001 composition is large, models are calculated against the average value (orange dashed

1002 lines) as well as the high and low ends of the values (grey dashed lines). **(b)** The
1003 impact of hydrothermal Ba input on the distribution of deep-water [Ba] and $\delta^{138/134}Ba$
1004 (Fig. 1). The dashed lines show the fraction of hydrothermal Ba input (F_{Ba_hyd}) in the
1005 deep water Ba (0-10%). The fraction values on display are calculated against the
1006 average hydrothermal $\delta^{138/134}Ba$ (+1.7‰). The original data of the yellow square
1007 shown in (a) is highlighted in the yellow area.
1008
1009 **Figure 8.** Relationship between seawater SO_4 concentrations and the input
1010 compositions of effective hydrothermal Ba ($[Ba]_{hyd}$ and $\delta^{138/134}Ba_{hyd}$) in the ocean.
1011 The yellow curve shows $[Ba]_{hyd}$, based on the barite saturation model ($\Omega_{barite} = 1$) at
1012 deep-water T-P condition (1°C and 500bar) (Monnin, 1999). The blue curve shows
1013 $\delta^{138/134}Ba_{hyd}$ with uncertainties (the grey curves), based on a fractionation factor
1014 ($\Delta^{138/134}Ba_{hyd\text{-}barite\text{-}fluid} = -0.35 \pm 0.10$ ‰) and $[Ba]_{hyd}$ in the Ba isotope fractionation
1015 model. For illustrative purposes, the initial composition for the fractionation is taken
1016 from the average values of endmember fluids (Table 3) as a generic composition
1017 ([Ba] = 42 μmol/kg and $\delta^{138/134}Ba$ = -0.07 ‰).

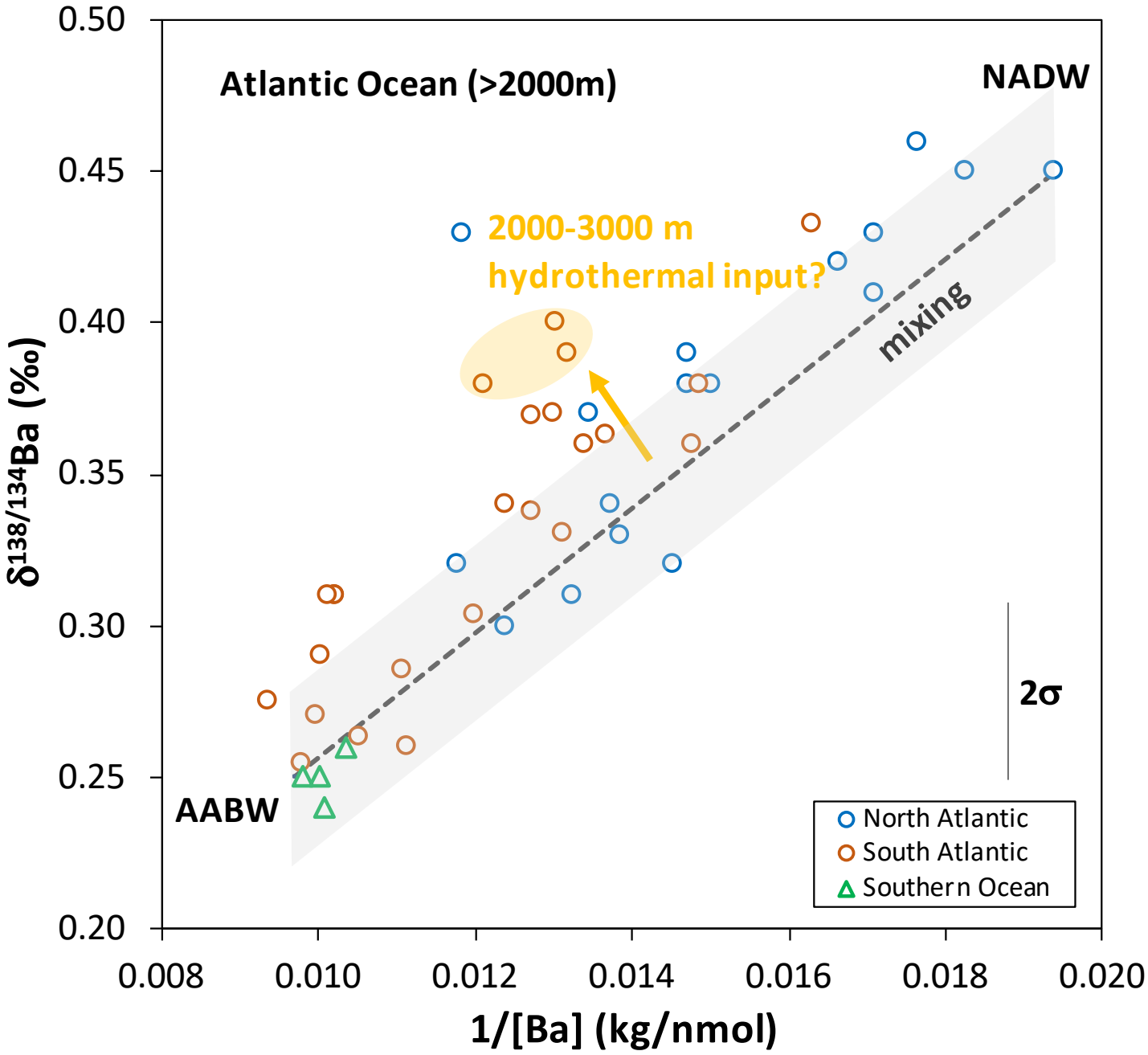
Atlantic Ocean (>2000m)
NADW
2000-3000 m
hydrothermal input?
mixing
AABW
2σ
North Atlantic
South Atlantic
Southern Ocean
δ138/134Ba (‰)
1/[Ba] (kg/nmol)
0.50
0.45
0.40
0.35
0.30
0.25
0.20
0.008
0.010
0.012
0.014
0.016
0.018
0.020

Figure 1

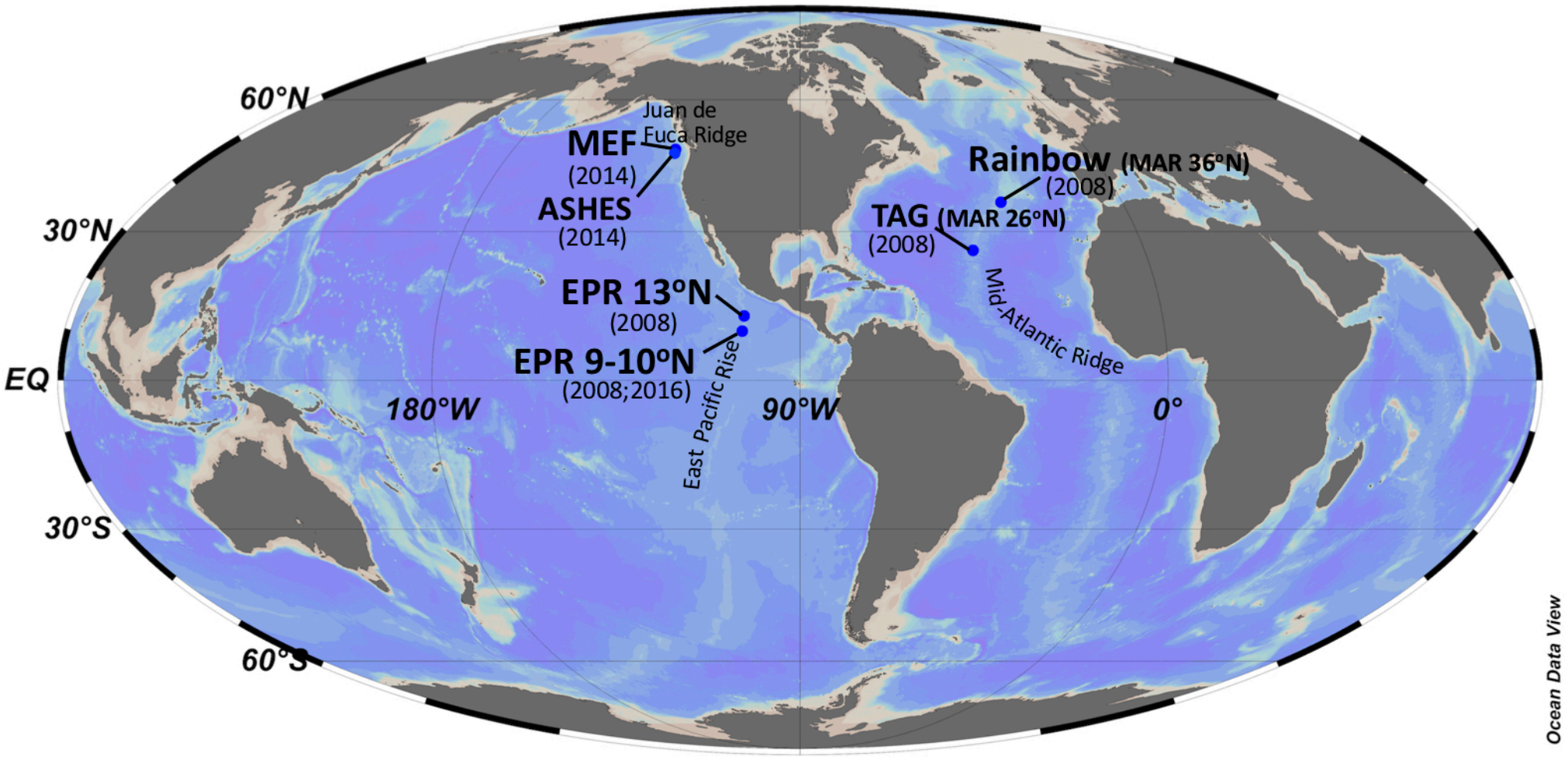
60°N
30°N
EQ
30°S
60°S
180°W
90°W
0°
Juan de Fuca Ridge
MEF
(2014)
ASHES
(2014)
Rainbow (MAR 36°N)
(2008)
TAG (MAR 26°N)
(2008)
EPR 13°N
(2008)
EPR 9-10°N
(2008;2016)
East Pacific Rise
Mid-Atlantic Ridge
Ocean Data View

Figure 2

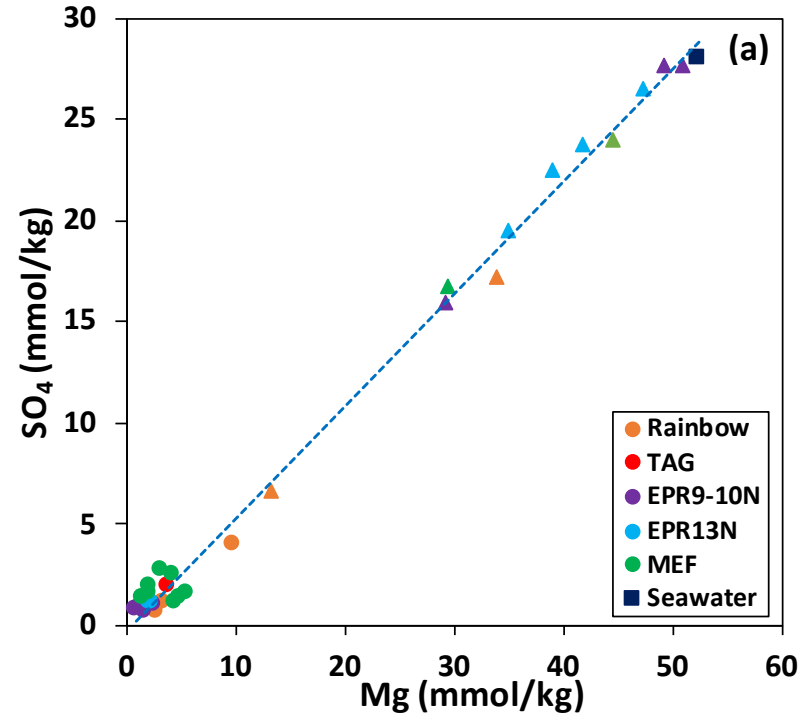
(a)
SO4 (mmol/kg)
Mg (mmol/kg)
Rainbow
TAG
EPR9-10N
EPR13N
MEF
Seawater

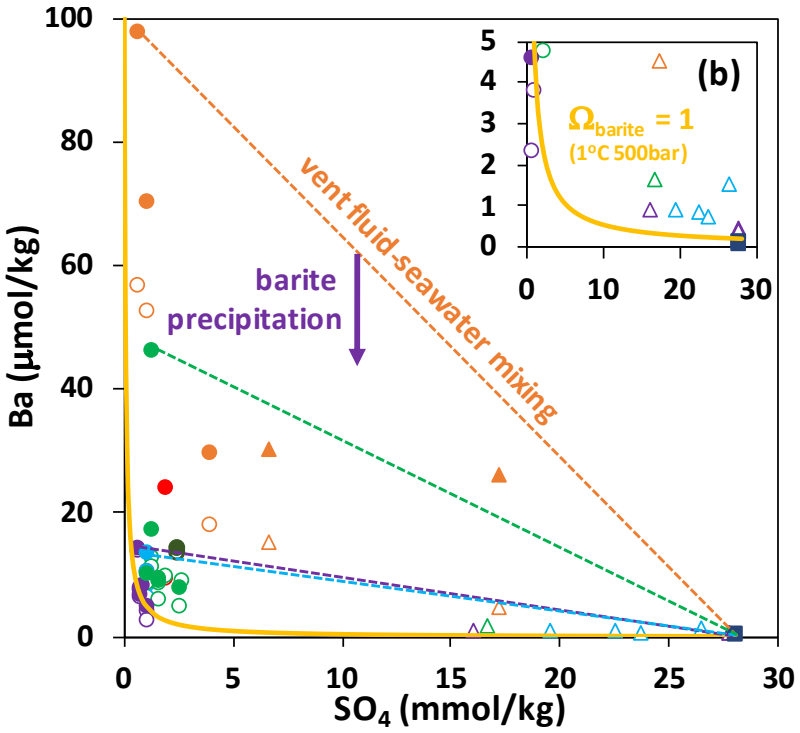
(b)
Ωbarite = 1
(1°C 500bar)
vent fluid-seawater mixing
barite
precipitation
Ba (µmol/kg)
SO4 (mmol/kg)

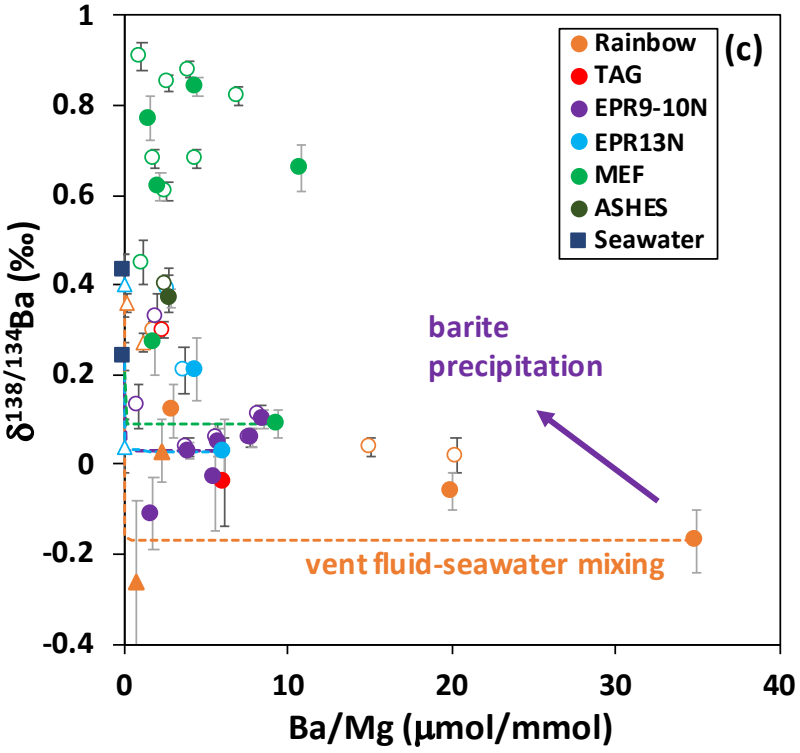
(c)
Rainbow
TAG
EPR9-10N
EPR13N
MEF
ASHES
Seawater
barite
precipitation
vent fluid-seawater mixing
δ138/134Ba (‰)
Ba/Mg (µmol/mmol)

Figure 3

Figure 4

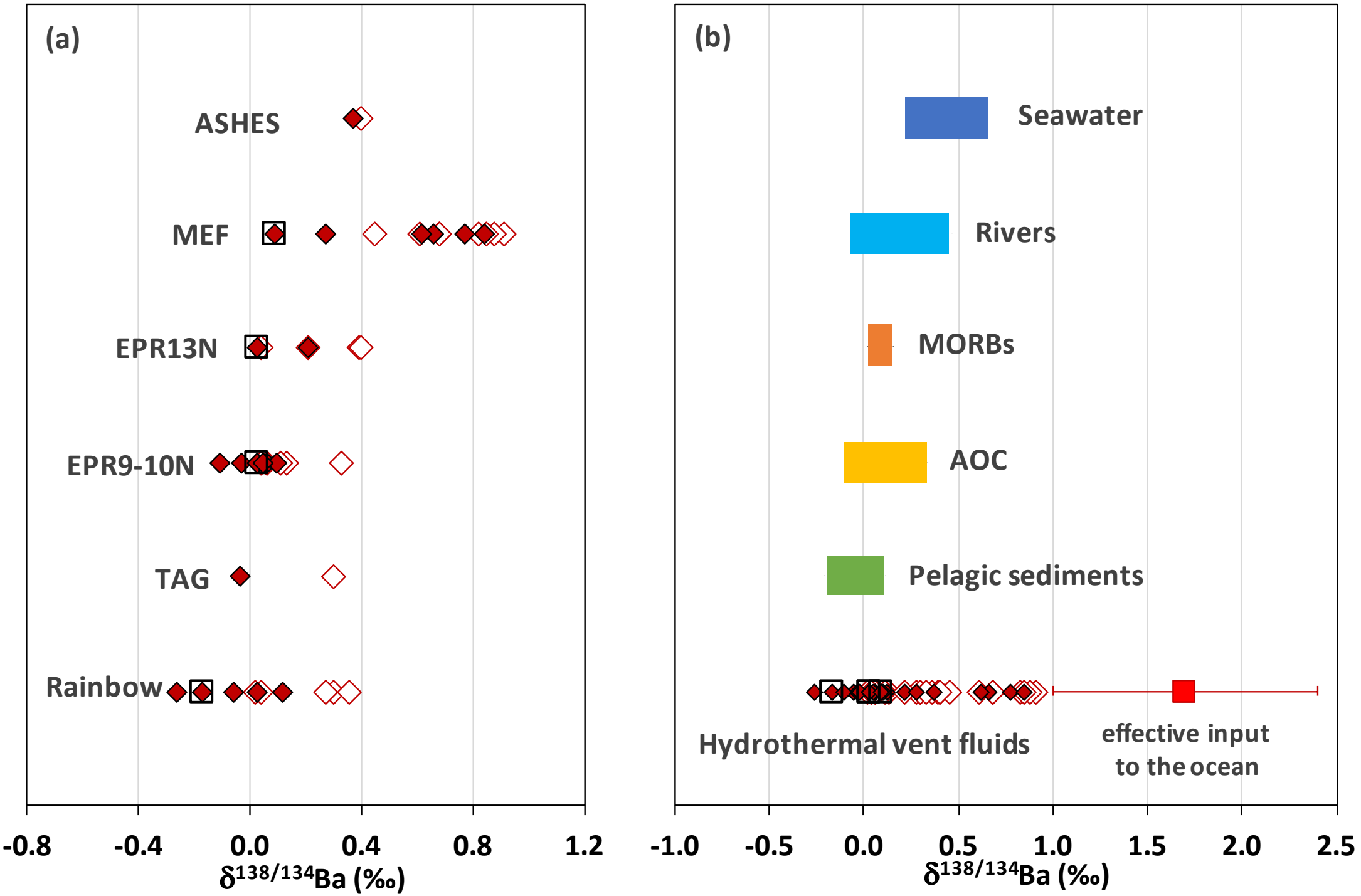
(a)
ASHES
MEF
EPR13N
EPR9-10N
TAG
Rainbow
-0.8
-0.4
0.0
0.4
0.8
1.2
δ138/134Ba (‰)
(b)
Seawater
Rivers
MORBs
AOC
Pelagic sediments
Hydrothermal vent fluids
effective input
to the ocean
-1.0
-0.5
0.0
0.5
1.0
1.5
2.0
2.5
δ138/134Ba (‰)

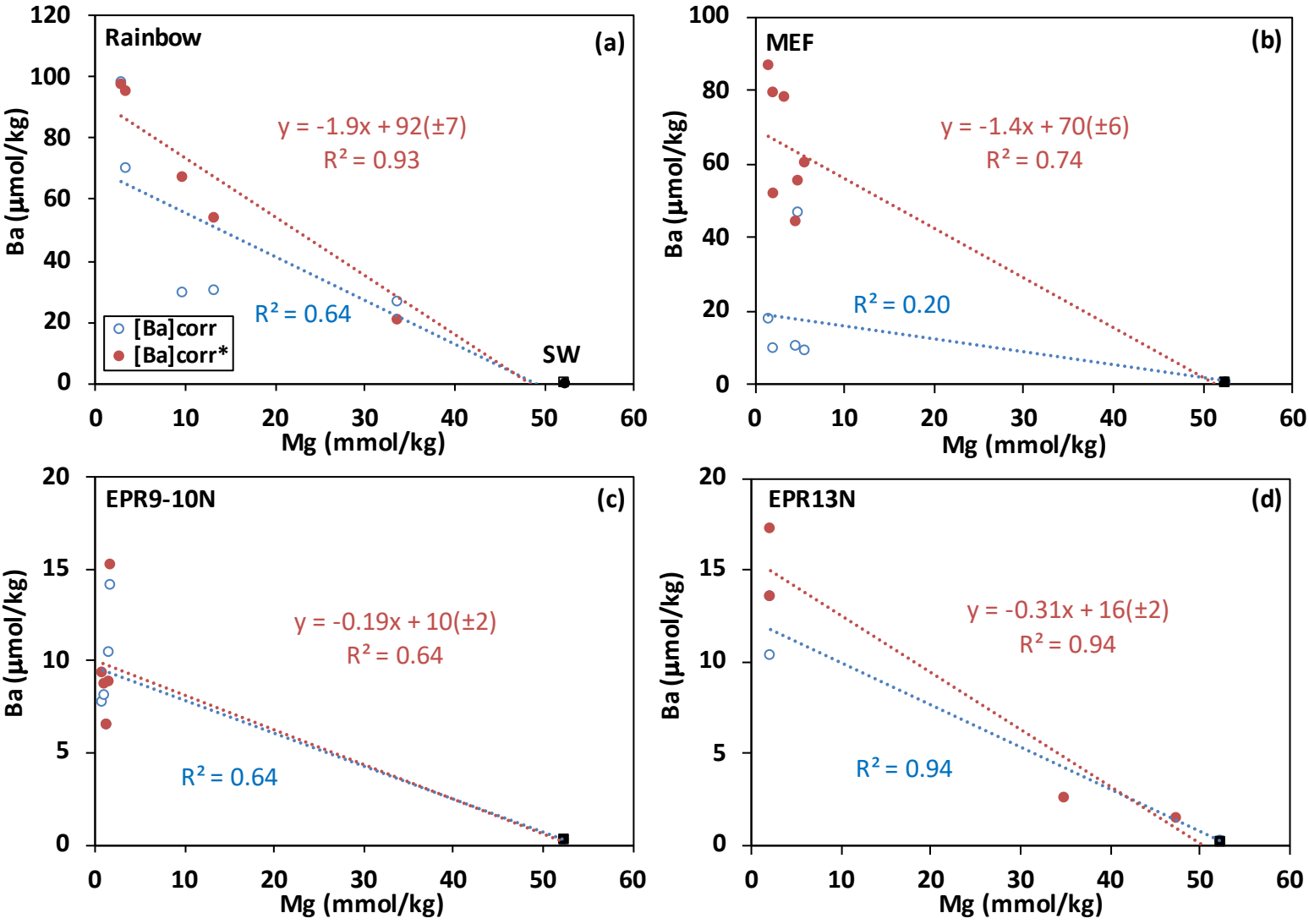
Rainbow
(a)
y = -1.9x + 92(±7)
R² = 0.93
R² = 0.64
[Ba]corr
[Ba]corr*
SW
Ba (µmol/kg)
Mg (mmol/kg)
MEF
(b)
y = -1.4x + 70(±6)
R² = 0.74
R² = 0.20
EPR9-10N
(c)
y = -0.19x + 10(±2)
R² = 0.64
R² = 0.64
EPR13N
(d)
y = -0.31x + 16(±2)
R² = 0.94
R² = 0.94

Figure 5

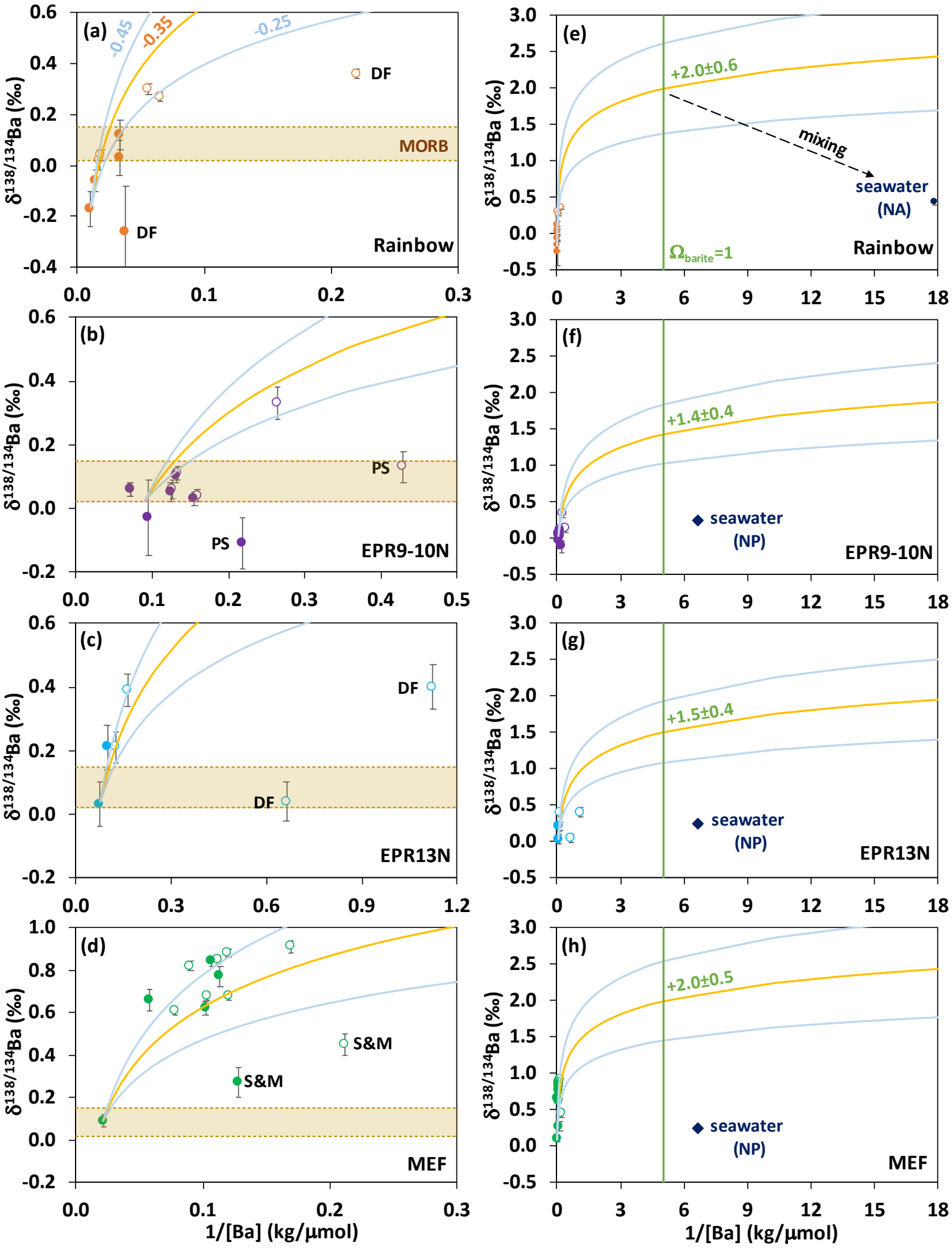
(a)
-0.45
-0.35
-0.25
DF
MORB
DF
Rainbow
(b)
PS
PS
EPR9-10N
(c)
DF
DF
EPR13N
(d)
S&M
S&M
MEF
(e)
+2.0±0.6
mixing
seawater
(NA)
Ω barite=1
Rainbow
(f)
+1.4±0.4
seawater
(NP)
EPR9-10N
(g)
+1.5±0.4
seawater
(NP)
EPR13N
(h)
+2.0±0.5
seawater
(NP)
MEF
δ138/134Ba (‰)
1/[Ba] (kg/µmol)

Figure 6

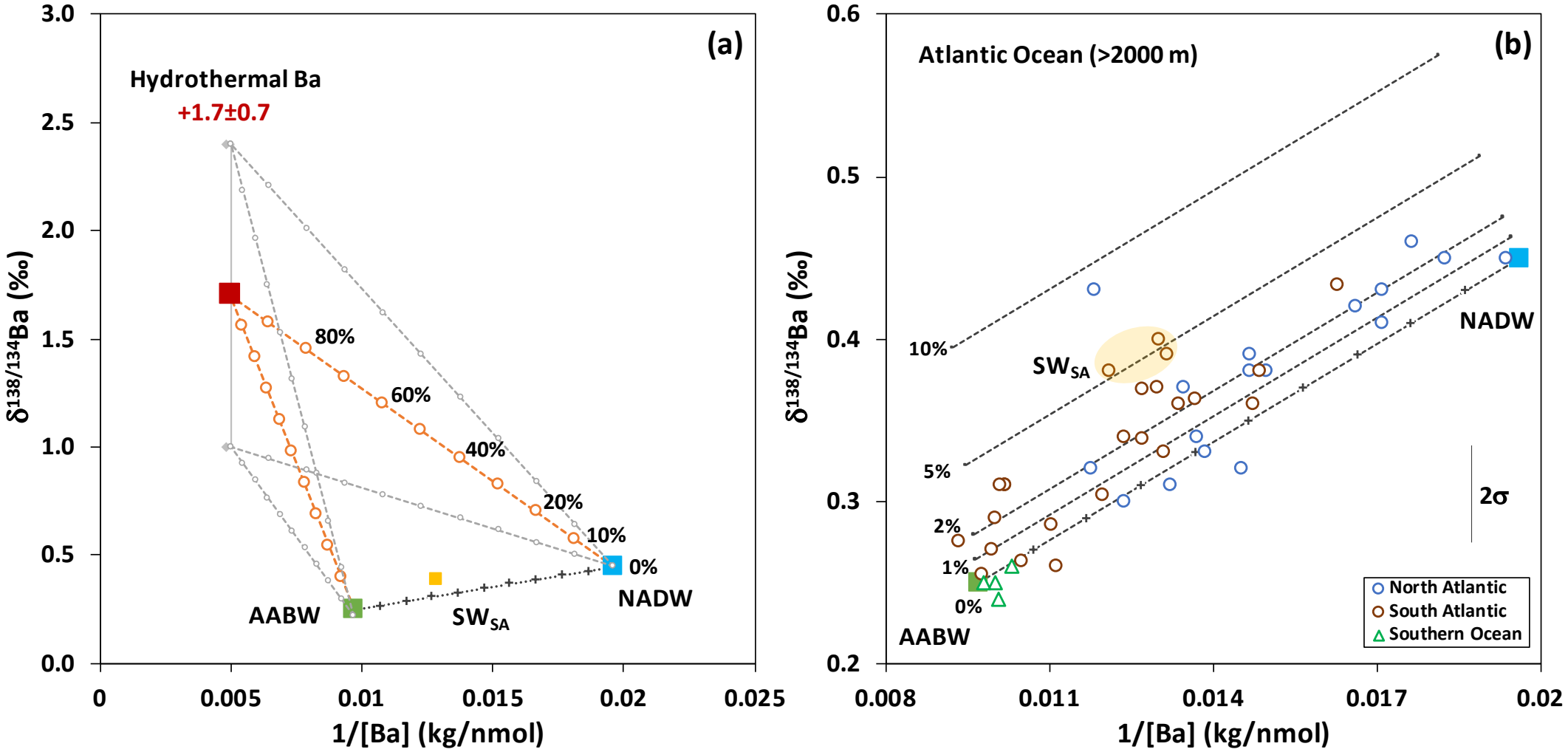
(a)
Hydrothermal Ba
+1.7±0.7
80%
60%
40%
20%
10%
0%
AABW
SW$_{SA}$
NADW
$\delta^{138/134}$Ba (‰)
1/[Ba] (kg/nmol)
3.0
2.5
2.0
1.5
1.0
0.5
0.0
0
0.005
0.01
0.015
0.02
0.025
(b)
Atlantic Ocean (>2000 m)
10%
5%
2%
1%
0%
SW$_{SA}$
NADW
AABW
2σ
North Atlantic
South Atlantic
Southern Ocean
$\delta^{138/134}$Ba (‰)
1/[Ba] (kg/nmol)
0.6
0.5
0.4
0.3
0.2
0.008
0.011
0.014
0.017
0.02

Figure 7

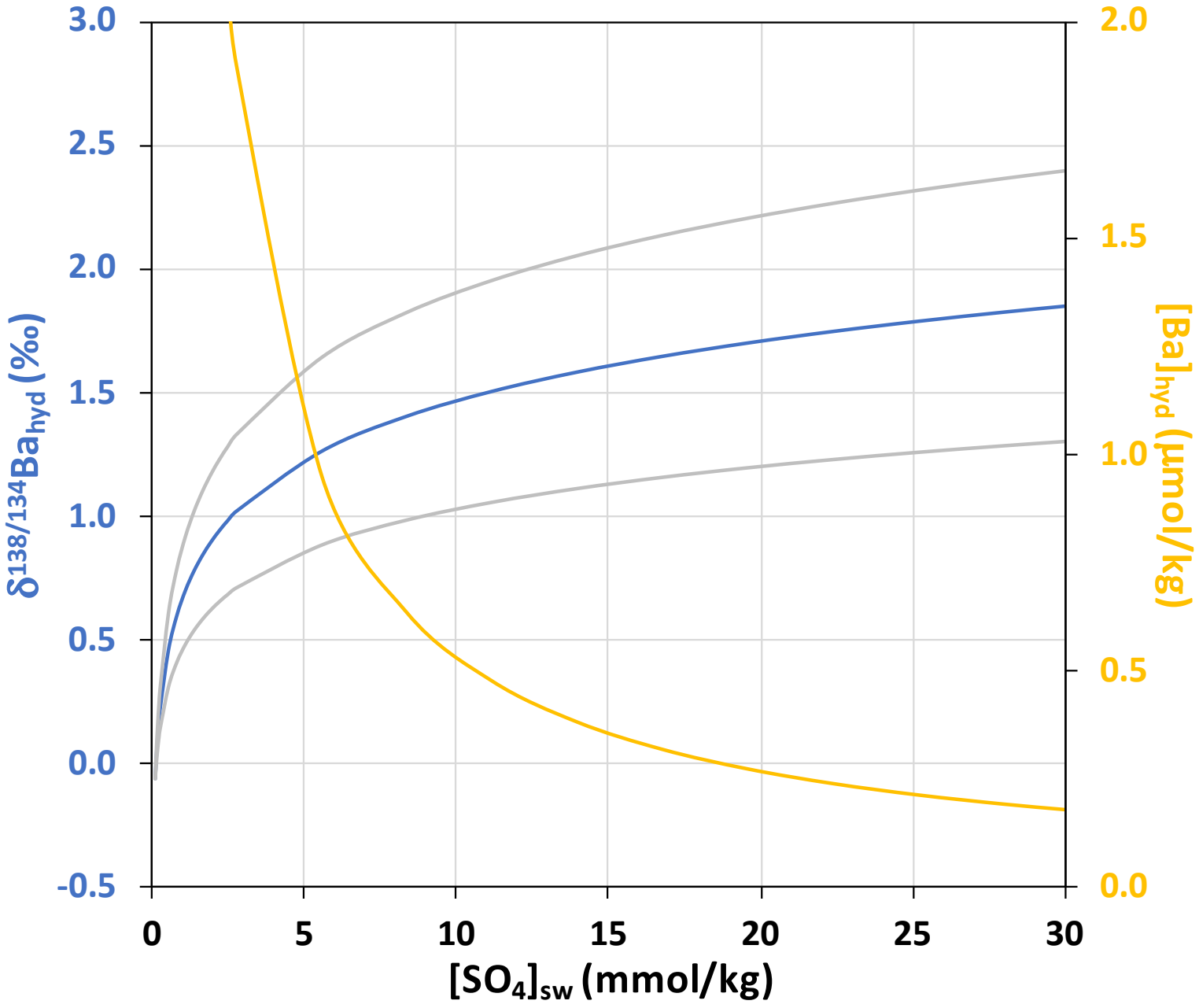
3.0
2.5
2.0
1.5
1.0
0.5
0.0
-0.5
δ138/134Bahyd (‰)
2.0
1.5
1.0
0.5
0.0
[Ba]hyd (µmol/kg)
0
5
10
15
20
25
30
[SO4]sw (mmol/kg)

Figure 8